Chinese Journal of
POLYMER SCIENCE

RESEARCH ARTICLE

https://doi.org/10.1007/s10118-026-3833-0
Chinese J. Polym. Sci.

Soft and Rigid Imide-based Benzoxazines as Precursors to High-performance Polybenzoxazines: Synthesis, Thermal Behavior, and Tunable Photoluminescent Properties

Abdulsalam Mahdy[a,b,c*], Jalal A. Zahra[a], Hassan K. Juwhari[d], Ruba I. Alzubi[e], and Osama Younis[f,g*]

[a] *Chemistry Department, School of Science, The University of Jordan, Amman 11942, Jordan*
[b] *Chemistry Department, Faculty of Education & Science, Rada'a, Albaydha University, Albaydha, Yemen*
[c] *Department of Pharmacy, Faculty of Medicine and Health Sciences, Ar-Rasheed Smart University, Sana'a, Yemen*
[d] *Department of Physics, School of Science, The University of Jordan, Amman 11942, Jordan*
[e] *Jordan Atomic Energy Commission, Amman 11934, Jordan*
[f] *Chemistry Department, Faculty of Science, New Valley University, El-Kharga 72511, Egypt*
[g] *Polymer Institute, Slovak Academy of Sciences, Dúbravská cesta 9, 84541, Bratislava, Slovakia*

Electronic Supplementary Information

Abstract Two new imide-functional benzoxazine monomers, **IBZ-EDA** and **IBZ-PHDA**, with distinct molecular architectures, were synthesized *via* a one-pot Mannich condensation reaction using ortho-phthalimide-functional phenol, paraformaldehyde, and either ethylenediamine or *para*-phenylenediamine as flexible and rigid bridging units, respectively. The chemical structures of the synthesized monomers were confirmed by Fourier transform infrared spectroscopy (FTIR), proton nuclear magnetic resonance spectroscopy (^{1}H-NMR), Carbon-13 (^{13}C)-NMR, distortionless enhancement by polarization transfer (DEPT-135), correlation spectroscopy (COSY), heteronuclear single quantum coherence (HSQC), heteronuclear multiple bond correlation (HMBC), and mass spectrometry analyses. Thermal ring-opening polymerization of the monomers produced highly crosslinked polybenzoxazine networks, **Poly(IBZ-EDA)** and **Poly(IBZ-PHDA)**, whose curing behaviors were investigated using DSC and FTIR. The flexible **IBZ-EDA** monomer exhibited a lower polymerization temperature owing to the proximity of the oxazine rings and favorable intramolecular interactions, whereas the rigid aromatic **IBZ-PHDA** structure required a higher curing temperature. Thermogravimetric analysis demonstrated substantial improvements in thermal stability after curing, with **Poly(IBZ-PHDA)** exhibiting outstanding performance, including T_{10} values up to 559 °C, a char yield of 79%, and a limiting oxygen index of 49.1%, reflecting its highly flame-retardant nature. Scanning electron microscopy (SEM) analysis revealed dense and highly crosslinked morphologies with structural differences arising from the flexibility of the diamine spacer. Photophysical investigations in the solution and solid states revealed complex excitation-dependent fluorescence behaviors for both monomers and polymers. The emission properties were strongly influenced by concentration, excitation wavelength, molecular packing, and polymer network formation. Dual-emission characteristics, broad chromaticity tunability, and multiple emissive states are observed, indicating the coexistence of locally excited, aggregated, and cluster-associated emissive species. Polymerization further alters the excited-state landscape through enhanced intermolecular interactions and restricted molecular motion. The results demonstrate that linker rigidity plays a critical role in controlling both the thermal and photophysical properties, providing an effective strategy for designing multifunctional polybenzoxazines with exceptional thermal stability, flame retardancy, and tunable luminescence.

Keywords Ring-opening polymerization; Polybenzoxazine; Thermal stability; Excitation-dependent emission; Solid-state luminescence

Citation: Mahdy, A.; Zahra, J. A.; Juwhari, H. K.; Alzubi, R. I.; Younis, O. Soft and rigid imide-based benzoxazines as precursors to high-performance polybenzoxazines: synthesis, thermal behavior, and tunable photoluminescent properties. *Chinese J. Polym. Sci.* https://doi.org/10.1007/s10118-026-3833-0

INTRODUCTION

Recent advances in sustainable polymer chemistry have further expanded the design space for high-performance thermosets, with emerging strategies focusing on renewable feedstocks, dynamic covalent chemistry, and multifunctional material platforms.[1–3] Polybenzoxazines (PBZs) are a class of advanced thermosetting polymers renowned for their exceptional thermal stability, mechanical strength, and versatile application potential. Their advantageous properties, including low water uptake, excellent dimensional stability, and remarkable chemical resistance, make them particularly attractive for aerospace, electronics, and sustainable material applications.[4–14] Recent research

* Corresponding authors, E-mail: abdualsalam735@gmail.com, abdualsalamaljbri@baydaauniv.net (A.M.)
E-mail: osamayounis@sci.nvu.edu.eg (O.Y.)
Received July 16, 2026; Accepted August 4, 2026; Published online September 28, 2026

has further expanded their utility through novel formulations targeting sustainability, nanocomposites, enhanced thermal and mechanical performance, shape-memory behavior, and smart materials.[15–17] PBZs were synthesized by ring-opening polymerization (ROP) of benzoxazine monomers upon thermal curing. This process yields highly crosslinked networks renowned for their exceptional thermal stability, inherent flame resistance, and superior mechanical strength.[18,19] During the polymerization of 3,4-dihydro-1,3-benzoxazines, two distinct polymer architectures can emerge, depending on the nucleophilic atom that attacks the electrophilic methylene group (NCH_2O). If the phenolic oxygen initiates the attack, N,O-acetal linkages corresponding to phenoxy-type structures are formed first. These intermediates may then undergo rearrangement to yield Mannich-type structures featuring free phenolic groups, known as phenol-type structures.[20,21]

The ROP of benzoxazines typically generates phenolic species *via* nucleophilic or electrophilic attacks at the *ortho* or *para* positions relative to the oxygen atom.[19,20] The resulting polybenzoxazine networks were characterized by extensive intra- and inter-molecular hydrogen bonding involving phenolic —OH groups, amine nitrogens, ether oxygens, and aromatic π-systems. This hydrogen-bonded architecture underpins the outstanding thermal stability, mechanical robustness, and long-term durability of the materials.[21–25]

Therefore, considerable research has focused on molecular design strategies that introduce functional groups or polymerizable moieties into benzoxazine structures. Among these, the incorporation of imide rings has proven particularly effective because of the rigid aromatic character, high thermal stability, and strong intermolecular interactions imparted by the imide groups. Imide-containing benzoxazines exhibit enhanced glass transition temperatures (T_g), improved char yields, and superior flame retardancy.[26] However, most reported systems are either monofunctional or exhibit limited structural diversity, which restricts their capacity to form highly crosslinked networks and achieve a balanced multifunctional performance. This limitation is increasingly significant, given the growing demand for multifunctional materials that integrate thermal resistance, flame retardancy, and optical functionality, particularly for applications in optoelectronics, high-temperature sensors, and flame-resistant coatings.[27]

Recent advances have yielded a new class of highly stable PBZs derived from the thermal conversion of *ortho*-functional benzoxazines.[28–30] Compared to conventional polybenzoxazines based on *para*-functional analogs, these ortho-functional polymers exhibit superior thermal properties, including higher glass transition temperatures and enhanced thermal stability. Several studies have described the synthesis of *ortho*-functional polybenzoxazines containing amic acid, amide, imide, and amide–imide groups.[31–34] These materials typically combine high thermal stability with outstanding molecular design flexibility and cost-effectiveness. Furthermore, incorporating benzoxazine moieties into polyimides can enhance dimensional stability, glass transition temperatures, surface hydrophobicity (as reflected in contact angles), and overall thermal stability.[35] Novel 1,3-benzoxazine monomers containing ortho-imide and benzocyclobutene functionalities (oHPNI-abcb and oPP-abcb) were synthesized.[28]

Notably, poly(oHPNI-abcb) demonstrated excellent thermal stability with decomposition temperatures T_{d5} of 405 °C and T_{d10} of 448 °C, whereas poly(oPP-abcb) exhibited a char yield (Yc @800°C) exceeding 60%. More recently, a novel ortho-phthalimide-functionalized benzoxazine monomer bearing an *ortho*-nitrile group was developed to investigate the thermally induced transformation of a benzoxazine resin into crosslinked polybenzoxazole.[26] The resulting material exhibited outstanding thermal performance, T_{d5} of 550 °C, char yield of 70%, and a remarkably low total heat release (7.6 kJ/g), demonstrating its potential as a high-performance, flame-resistant material. Although relatively unexplored, fluorescent polybenzoxazines offer significant promise for applications, such as nondestructive damage sensing, anticounterfeiting, and structural health monitoring. Nevertheless, simultaneously optimizing the thermal, flame-retardant, and photophysical properties within a single PBZ platform remains a considerable challenge.[4,36–38]

Despite the remarkable progress achieved in benzoxazine chemistry and other optical materials,[39–43] studies integrating imide-functionalized benzoxazines with comprehensive investigations of their thermal, morphological, and photophysical properties remain relatively scarce. In particular, the influence of molecular flexibility and rigidity on polymerization behavior, thermal stability, flame-retardant performance, and excitation-dependent luminescence has not been systematically explored. To address this gap, two new difunctional imide-functional benzoxazine monomers, **IBZ-EDA** and **IBZ-PHDA**, were synthesized using ethylenediamine and *para*-phenylenediamine (**PHDA**) linkers, respectively. The resulting monomers were structurally characterized by Fourier transform infrared spectroscopy (FTIR), nuclear magnetic resonance (NMR), and mass spectrometry and subsequently converted into their corresponding polybenzoxazines through thermal ring-opening polymerization. The effects of the linker structure on the curing behavior, thermal stability, flame retardancy, and microstructural morphology were investigated using FTIR, thermogravimetric analysis (TGA), differential scanning calorimetry (DSC), and scanning electron microscopy (SEM) analyses. Furthermore, detailed solution-state and solid-state photophysical studies were conducted to elucidate the role of the molecular architecture and polymer network formation in the generation of emissive states and excitation-dependent fluorescence. This study provides valuable insights into the design of multifunctional imide-containing polybenzoxazines that combine exceptional thermal performance with tunable luminescence.

EXPERIMENTAL

Materials and Characterization Techniques

ortho-Phthalimide functional phenol (*O*-PP) was synthesized in our laboratory following a previously reported procedure.[13] Ethylenediamine (EDA, 98%) and *para*-phenylenediamine (99%) were obtained from Thermo Fisher Scientific (Germany) and were used as received. All solvents, including toluene, ethanol, hexane, ethyl acetate, methanol, and chloroform, were used as received without further purification.

^{1}H, ^{13}C, and DEPT-135 NMR spectra were obtained on a

https://doi.org/10.1007/s10118-026-3833-0

Bruker Avance-III 500 MHz spectrometer in dimethyl sulfoxide (DMSO-d_6) at 25 °C, with tetramethylsilane (TMS) as the internal standard. FTIR spectra were recorded on a Mattson 1000 spectrometer over the range of 400–4000 cm^{-1} to identify characteristic functional groups. The thermal stability of the prepared samples was evaluated by TGA using a Netzsch STA 409 PG/PC instrument under nitrogen atmosphere. The measurements were carried out at a heating rate of 10 °C/min from room temperature to 800 °C. Polymerization behavior was evaluated using DSC-TA Instruments Q2000). Each test specimen was subjected to two heating–cooling cycles from 0 °C to 350 °C at a heating rate of 10 °C/min under a nitrogen atmosphere.

High-resolution mass spectrometry (HRMS) measurements were carried out in the positive electrospray ionization (ESI^+) mode using a Bruker APEX-IV (7 T) mass spectrometer. The surface morphology was examined by SEM (Hitachi), and the crystallinity was investigated by X-ray diffraction (XRD) using a Rigaku D_{max} diffractometer with Cu Kα radiation (λ=1.5404 Å). Ultraviolet-visible (UV-Vis) absorption spectra were recorded using an Agilent 8453 spectrophotometer.

Steady-state photoluminescence (PL) spectra were obtained using an Eclipse fluorescence spectrophotometer equipped with a xenon lamp excitation source, automatic filter wheels, and a reference detector for real-time correction of excitation-source intensity fluctuations. Long-pass filters were used in the emission path to block the scattered excitation light. The emission spectra were corrected for the wavelength-dependent sensitivity of the detection system using a calibrated standard lamp, and the instrument software automatically applied correction factors. Control measurements on neat *N*,*N*-dimethylformamide (DMF, for solution samples) and bare quartz slides (for solid-state samples) showed no detectable emissions, confirming that the observed signals originated from the materials under investigation.

All PL solid-state measurements were performed on powder samples placed on quartz slides using long-pass filters in the emission path to block scattered excitation light. The control measurements on bare quartz slides showed no detectable emissions under identical conditions. Measurements were performed in DMF solution for the monomeric samples and in the solid state for both monomers and the corresponding polymer.

For PL measurements of samples with high absorbance (10^{-4} mol/L), a triangular (front-face) fluorescence cell was used to minimize the inner-filter effects and reabsorption. In this geometry, the excitation beam is directed at a small angle to the sample surface, and the emitted light is collected from the same side (front-face detection), thereby significantly reducing the effective path length through the sample. The Commission Internationale de l'Éclairage (CIE) chromaticity coordinates were calculated from the emission spectra that were corrected for the wavelength-dependent sensitivity of the detection system using a calibrated standard lamp. Correction factors were applied automatically using instrument software.

Synthesis of 2,2'-(Ethane-1,2-diylbis(3,4-dihydro-2*H*-benzo[e][1,3]oxazine-3,8-diyl))bis(isoindoline-1,3-dione) (IBZ-EDA)

The **IBZ-EDA** monomer was prepared according to a previously reported procedure with minor modifications.[44] A mixture of ethylenediamine (0.120 g, 2 mmol), *O*-PP (0.957 g, 4 mmol), paraformaldehyde (0.240 g, 8 mmol), and 30 mL of a toluene/ethanol mixture (2/1, *V*/*V*) was placed in a 100 mL one-necked round-bottom flask. The mixture was heated under reflux at 90 °C with continuous stirring. The reaction progress was monitored by thin-layer chromatography (TLC) using hexane/chloroform (5/2, *V*/*V*) as the eluent. After 7 h, the reaction mixture was cooled to room temperature, filtered, and washed again with cold methanol. The resulting solid was dried to obtain the difunctional benzoxazine monomer, hereafter designated as **IBZ-EDA**.

Yield: 83%. Appearance: off-white. FTIR (cm^{-1}): 915, 1112, 1226, 1721, 1768. ^{13}C-NMR (500 MHz, DMSO-d_6, δ, ppm): 49.45 (s, 2C, methylene amine chain), 49.54 (s, 2C, —N—CH_2—Ar—), 79.62 and 83.64 ppm (s, 2C, —N—CH_2—O), 119–135 and 150.6 (S, 24C, aromatic C), 167.3 (s, 4C, C=O imide). ^{1}H-NMR (500 MHz, DMSO-d_6, δ, ppm): 3.41(s, 4H, methylene amine chain), 4.61 (s, 4H, —N—CH_2—Ar), 5.400 (s, 4H, —N—CH_2—O—), 7.5–8.8 (s, 12H, aromatic H). HRMS (ESI): m/z 609.17446 ($[M+Na]^+$), calcd for $C_{34}H_{26}N_4NaO_6$: 609.17446 (mass error: 0 ppm).

Synthesis of 2,2'-(1,4-Phenylenebis(3,4-dihydro-2*H*-benzo[e][1,3] oxazine-3,8-diyl))bis(isoindoline-1,3-dione)(IBZ-PHDA)

The **IBZ-PHDA** monomer was synthesized according to a previously reported procedure with minor modifications.[44] In a 100 mL one-necked round-bottom flask, a mixture of PHDA (0.216 g, 2 mmol), *O*-PP (0.957 g, 4 mmol), and paraformaldehyde (0.240 g, 8 mmol) was dissolved in a toluene/ethanol mixture (2/1, *V*/*V*). The solution was heated under reflux at 90 °C with continuous stirring. The reaction progress was monitored by thin-layer chromatography (TLC) using hexane/chloroform (5/2, *V*/*V*) as the eluent. After 24 h, the reaction mixture was cooled to room temperature, filtered, and washed again with cold methanol. The resulting solid was dried to obtain the difunctional benzoxazine monomer, hereafter designated as **IBZ-PHDA**.

Yield: 75%. Appearance: dark yellow. FTIR (cm^{-1}): 923, 1064, 1228, 1712, 1774. ^{13}C-NMR (500 MHz, DMSO-d_6, δ, ppm): 50.60/49.07 (w, 2C, —N—CH_2—Ar—), 82.42/80.06 (s, 2C, —N—CH_2—O), 117-154 (S, 30C, aromatic), 167.2–167.6 (s, 4C, C=O imide). ^{1}H-NMR (500 MHz, DMSO-d_6, δ, ppm): 4.63 (w, 4H, —N—CH_2—Ar), 5.32 (s, 4H, —N—CH_2—O—), 6.4–8.0 (s, 18H, aromatic H). HRMS (ESI): m/z 673.14839 ($[M + K]^+$), calcd for $C_{38}H_{26}N_4KO_6$: 673.14839 (mass error: 10.80 ppm).

Synthesis of Poly(IBZ-EDA) and Poly(IBZ-PHDA)

The synthesis of **Poly(IBZ-EDA)** and **Poly(IBZ-PHDA)** proceeds *via* the ROP of the corresponding benzoxazine monomers during thermal curing, as illustrated schematically in Scheme 1. The proposed network structures shown in Scheme 1 are schematic representations of the expected phenolic Mannich-type crosslinked architectures. The monomeric solids were placed on stainless steel and gradually heated in a forced air oven. The curing protocol consisted of sequential heating at 70, 100, 150, and 200 °C for **IBZ-EDA** and at 100, 150, 200, and 250 °C for **IBZ-PHDA**, with each step maintained for 2 h. The color change photographs obtained after this curing process are shown in Fig. S1 (in the electronic supplementary information, ESI), con-

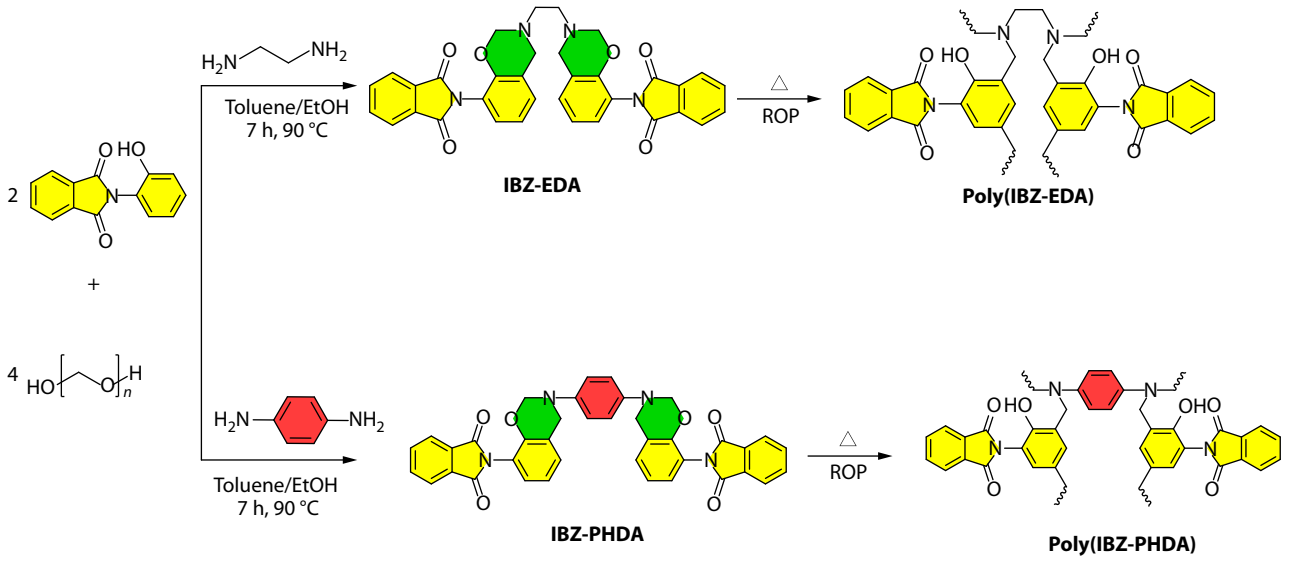

Scheme 1 The synthetic routes for the synthesis of **IBZ-EDA** and **IBZ-PHDA** using amine:phenol:formaldehyde = 1:2:4 stoichiometry, followed by ROP to produce **Poly(IBZ-EDA)** and **Poly(IBZ-PHDA)**. The cured network structures are depicted as schematic representations of the proposed phenolic Mannich-type crosslinked architecture.

firming progressive cross-linking and the formation of a phenolic Mannich-bridge network.

RESULTS AND DISCUSSION

Structural Characterization of IBZ-EDA and IBZ-PHDA

Soft and rigid imide-functional benzoxazine monomers with robust thermal stability were synthesized *via* a one-pot Mannich condensation (Scheme 1). The soft analog (**IBZ-EDA**) was prepared using ethylenediamine (EDA), while the rigid counterpart (**IBZ-PHDA**) was obtained using *para*-phenylenediamine. Both monomers were synthesized by reacting the corresponding diamines with *ortho*-phthalimide functional phenol (*O*-PP) and paraformaldehyde in a toluene/ethanol co-solvent mixture (2/1, *V*/*V*).

The longer reaction time required for **IBZ-PHDA** (24 h) compared to **IBZ-EDA** (7 h) is attributed to the lower nucleophilicity and reduced reactivity of aromatic *para*-phenylenediamine (PHDA) relative to aliphatic ethylenediamine (EDA). In PHDA, the amino groups are directly attached to an aromatic ring, resulting in electron delocalization through conjugation, which decreases the electron density on the nitrogen atoms and thus diminishes their nucleophilicity toward the electrophilic iminium intermediates formed during Mannich condensation. Additionally, the rigid and sterically demanding aromatic structure of PHDA imposes greater steric hindrance, further slowing condensation kinetics. In contrast, the aliphatic ethylenediamine in **IBZ-EDA** possesses highly nucleophilic primary amine groups with enhanced reactivity, enabling the faster formation of the bis-benzoxazine product. The progress of the reaction was monitored by TLC, and complete conversion of the less reactive PHDA required an extended reflux time to achieve comparable yields.

NMR for the Structural Characterization of IBZ-EDA and IBZ-PHDA

The chemical structures were confirmed through comprehensive NMR analysis, including one-dimensional (^{1}H, ^{13}C, DEPT-135) and two-dimensional (COSY, HSQC, and HMBC) experiments.

IBZ-EDA. The ^{1}H-NMR spectrum of **IBZ-EDA** (Fig. 1) displays aromatic proton signals in the range of δ=7.5–8.87 ppm, characteristic of the conjugated phenyl rings. Two equivalent signals at δ=4.6 and 5.4 ppm are assigned to the oxazine ring protons, corresponding to the Ar—CH_2—N and O—CH_2—N moieties, respectively. The signal at δ=3.4 ppm is attributed to the methylene protons of the ethylenediamine linker.[45] The ^{13}C-NMR spectrum displays aromatic carbon resonances in the range of δ=119–150 ppm and a sharp carbonyl signal at δ=167 ppm, confirming the presence of imide functionality. The methylene carbons of the oxazine ring appear at δ=83.6 ppm (O—CH_2—N) and δ=49.5 ppm (Ar—CH_2—N), while an additional signal at δ=49.45 ppm is assigned to the CH_2 groups of the diamine linker.[26] The DEPT-135 spectrum further supported these assignments, showing negative signals characteristic of the CH_2 groups.

Further validation was performed using 2D NMR analyses. The correlation spectroscopy (COSY) spectrum revealed coupling correlations between the oxazine methylene protons and adjacent aromatic protons. HSQC experiments confirmed the direct ^{1}H–^{13}C connectivity for the Ar—CH_2—N and O—CH_2—N carbons. HMBC long-range correlations between the methylene protons and aromatic carbons provided conclusive evidence for successful oxazine ring closure.

IBZ-PHDA. The ^{1}H-NMR spectrum of **IBZ-PHDA** (Fig. 2) displays characteristic aromatic proton signals as multiplets in the region of δ=6.3–8.0 ppm. The methylene protons of the oxazine ring appear as distinct broad signals at δ=5.32 ppm, corresponding to the O—CH_2—N moiety, and at δ=4.63 ppm, assigned to the Ar—CH_2—N group.[46] The ^{13}C-NMR spectrum reveals carbonyl carbon resonances at δ=167 ppm and aromatic carbon signals in the range δ=117–152 ppm. The oxazine ring methylene carbons were observed at δ=82/80 ppm (O—CH_2—N) and δ=50/49 ppm (Ar—CH_2—N). The pres-

https://doi.org/10.1007/s10118-026-3833-0

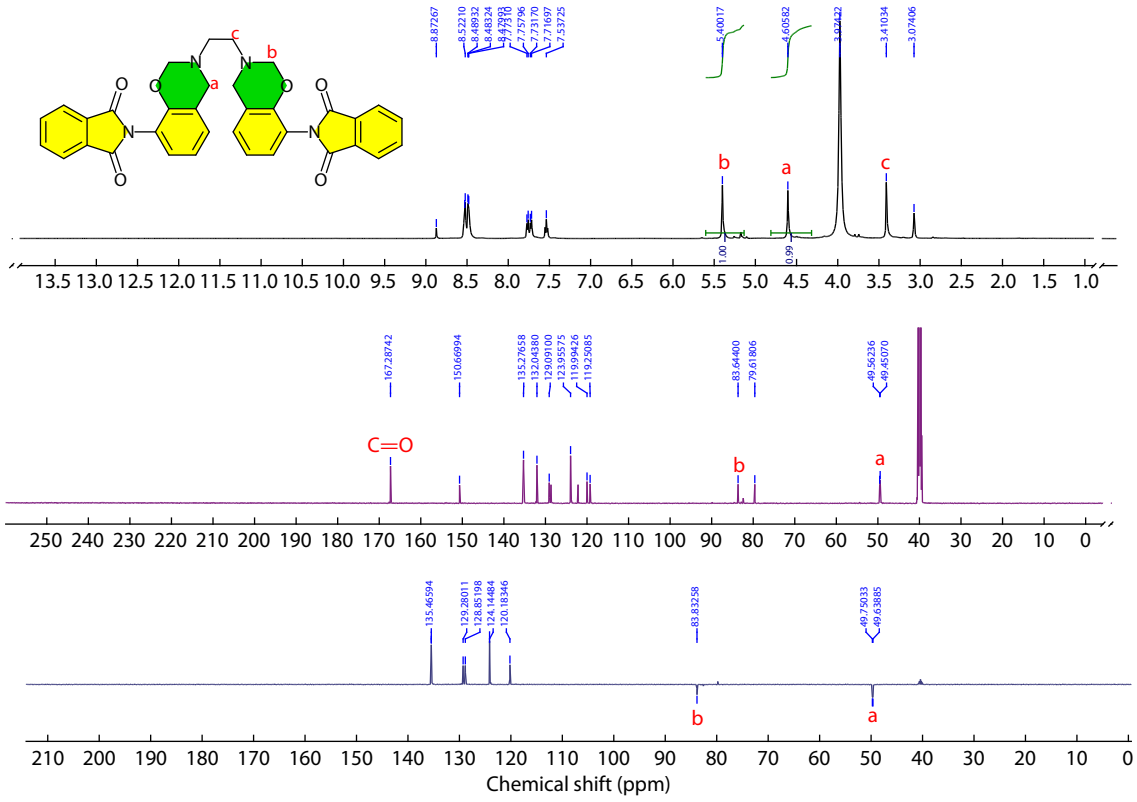

Fig. 1 ^{1}H, ^{13}C, DEPT-135 NMR spectra (500 MHz, DMSO-d_6) of **IBZ-EDA**.

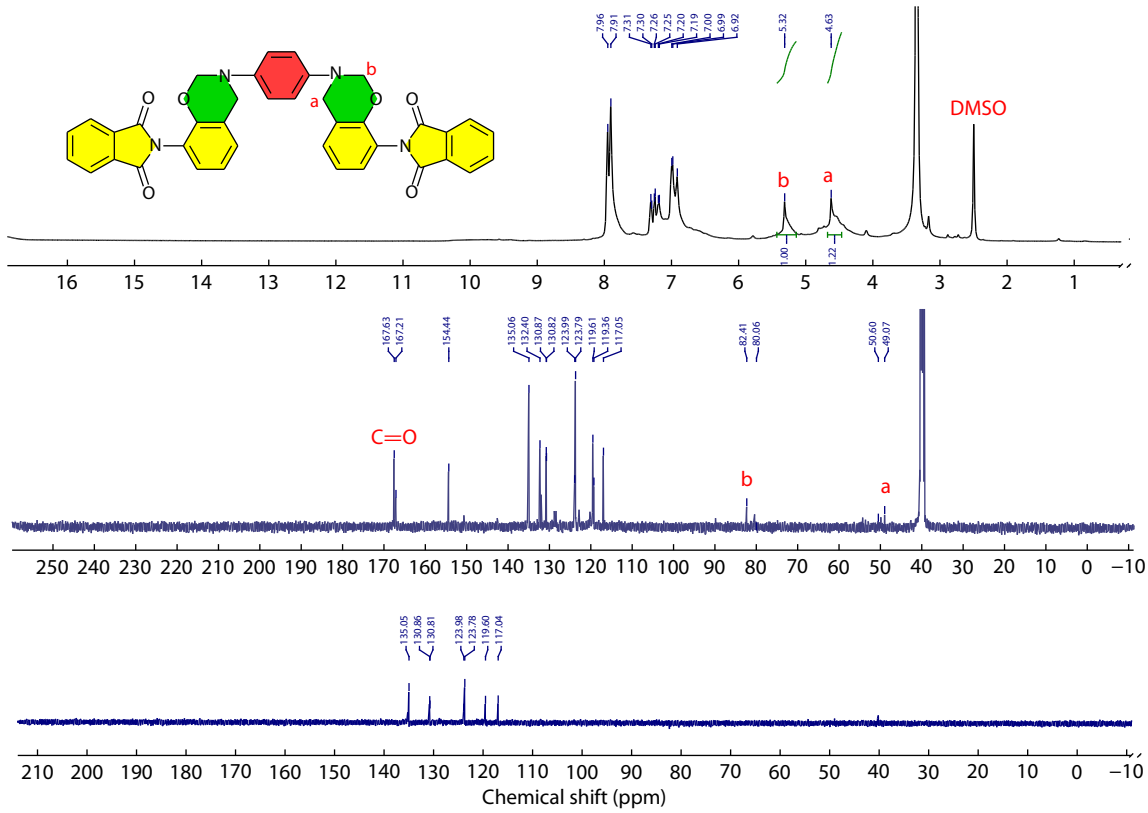

Fig. 2 ^{1}H, ^{13}C, DEPT-135 NMR spectra (500 MHz, DMSO-d_6) of **IBZ-PHDA**.

https://doi.org/10.1007/s10118-026-3833-0

ence of two distinct carbonyl signals at δ=167.6 and 167.2 ppm, along with the non-equivalent methylene environments, confirms the asymmetric nature of the benzoxazine unit. In the DEPT-135 spectrum, the absence of negative signals for methylene carbons may be attributed to the limited solubility of the compound, likely due to its high aromatic content. Collectively, the 1D and 2D (Figs. S2–S7 in ESI) NMR data were fully consistent with the proposed molecular structures, confirming the successful synthesis of both difunctional imide-based benzoxazine monomers.

FTIR for Structural Characterization of IBZ-EDA and IBZ-PHDA

FTIR spectroscopy was used to investigate the molecular structures of the synthesized monomers. Fig. 3 shows the FTIR spectra of **IBZ-EDA** and **IBZ-PHDA**, recorded at room temperature over the range of 500–3000 cm^{-1}. Characteristic benzoxazine ring vibrations were observed at 915, 1112, and 1226 cm^{-1} for **IBZ-EDA**, and at 923, 1064, and 1228 cm^{-1} for **IBZ-PHDA**, corresponding to C—O—C asymmetric stretching, C—N—C stretching, and oxazine ring modes, respectively.[47] In addition, the imide functionality was confirmed by the presence of two characteristic carbonyl stretching bands, attributed to asymmetric and symmetric C=O vibrations, at 1768 and 1721 cm^{-1} for **IBZ-EDA**, and at 1774 and 1712 cm^{-1} for **IBZ-PHDA**. The positions and intensities of these bands were in good agreement with previously reported data for imide-based benzoxazine monomers, confirming the successful formation of the target structures.[18,32]

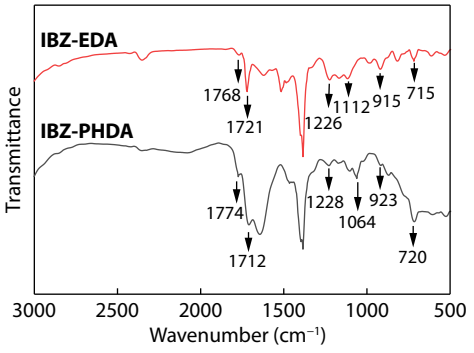

Fig. 3 Transmittance representative FTIR spectra of **IBZ-EDA** and **IBZ-PHDA** monomers.

Mass Spectrometry (MS) for Structural Characterization of IBZ-EDA and IBZ-PHDA

The chemical structures of the target monomers were further confirmed by mass spectrometry (MS) analysis. The MS spectrum of **IBZ-EDA** (Fig. S8 in ESI) exhibits a prominent molecular ion peak at *m/z*=609.17, corresponding to the sodium adduct $[M + Na]^+$ detected in positive-mode ESI–MS, which is consistent with the proposed molecular formula $C_{34}H_{26}N_4O_6Na$.[48] Similarly, the MS spectrum of **IBZ-PHDA** (Fig. S9 in ESI) displays a prominent molecular ion peak at *m/z*=673.15, attributed to the potassium adduct $[M+K]^+$, in agreement with the expected molecular formula $C_{38}H_{26}N_4O_6K$. The close match between the observed and calculated mass values confirmed the successful synthesis of both target compounds. Additionally, the fragment peaks observed at lower *m/z* values are consistent with the expected fragmentation patterns of the molecular frameworks, providing further support for the proposed structures.

High-resolution mass spectra were acquired with excellent mass accuracy. For **IBZ-EDA**, the observed *m/z* of 609.17446 for the sodium adduct $[M+Na]^+$ matches the calculated value of 609.17446 for $C_{34}H_{26}N_4NaO_6$, with a mass error of 0.0 ppm. For **IBZ-PHDA**, the observed *m/z* of 673.14839 for the potassium adduct $[M+K]^+$ matches the calculated value of 673.14839 for $C_{38}H_{26}N_4KO_6$, also with a mass error of 0.0 ppm. These mass errors were well within the accepted tolerance (<5 ppm) for high-resolution mass spectrometry, confirming the high accuracy of the measurements. Furthermore, the experimental isotope patterns for both adduct ions were in excellent agreement with the theoretical isotopic distributions calculated for the proposed molecular formulas, providing additional confirmation of the elemental composition.

Elemental analysis was performed for both monomers to provide an independent assessment of purity. For **IBZ-EDA** ($C_{34}H_{26}N_4O_6$): calculated C, 69.61%; H, 4.47%; N, 9.55%; found C, 69.48%; H, 4.52%; N, 9.48%. For **IBZ-PHDA** ($C_{38}H_{26}N_4O_6$): calculated C, 71.91%; H, 4.13%; N, 8.83%; found C, 71.82%; H, 4.18%; N, 8.76%. The excellent agreement between the calculated and found values confirms the high purity of both monomers and supports the proposed molecular formulas.

Thermal Polymerization of IBZ-EDA and IBZ-PHDA

The polymerization behavior of the target imide-functionalized benzoxazines, **IBZ-EDA** and **IBZ-PHDA**, were investigated using DSC and FTIR. Fig. 4(a) shows the DSC thermograms of **IBZ-EDA** at different curing stages (uncured, 110, 150, 170 and 200 °C). The uncured sample exhibits a distinct exothermic peak at approximately 189 °C, corresponding to the ROP of the oxazine moiety. As the curing temperature increased, this exothermic peak progressively reduced and completely disappeared at 150 °C, indicating full conversion of the monomer into a crosslinked polymer network. Notably, the observed polymerization temperature was lower than that of conventional benzoxazine systems, a feature attributed to the ethylenediamine bridge within the molecular structure.[49]

The short aliphatic chain of ethylenediamine brings the oxazine rings into close spatial proximity, promoting the formation of intra- and inter-molecular hydrogen bonds between the amine groups and oxygen or nitrogen atoms of the oxazine rings. These hydrogen-bonding interactions weaken the oxazine ring, thereby reducing the activation energy required for ring-opening and enabling polymerization at lower temperatures. This behavior is consistent with previous studies of diamine-based benzoxazines, where ethylenediamine, the shortest diamine chain, exhibited an exceptionally low onset polymerization temperature, as determined by DSC.[50] The absence of any further exothermic transitions confirmed the complete polymerization and formation of a thermally stable poly(imide-benzoxazine) network.

Fig. 4(b) presents the FTIR spectra of **IBZ-EDA** recorded at different curing temperatures (25, 100, 150 and 200 °C). The spectrum of the uncured monomer displays characteristic benzoxazine absorption bands at 1231 cm^{-1} (C—O—C asymmetric stretching), 952 and 1180 cm^{-1} (oxazine ring vibrations), and in the region 1335–1350 cm^{-1} (N—CH_2—O linkage).[51] These characteristic peaks gradually decreased in in-

tensity and completely disappeared upon heating to 150 °C, indicating the occurrence of ROP and the formation of a cross-linked polybenzoxazine network.

It should be noted that while the disappearance of the characteristic benzoxazine FTIR bands and the DSC exotherm confirmed the occurrence of ring-opening polymerization and crosslinking, the exact three-dimensional network topology could not be unambiguously determined from these data alone. Therefore, the structures depicted in Scheme 1 are schematic representations of the proposed phenolic Mannich-type network, consistent with the established polymerization mechanism of benzoxazines.

The polymerization behavior of **IBZ–PHDA** was similarly investigated using DSC and FTIR (Fig. 5). Fig. 5(a) shows the DSC thermograms recorded at various curing temperatures (25–250 °C), revealing a prominent exotherm in the range 247–257 °C, attributed to benzoxazine ROP. The higher rigidity and aromatic content of the *para*-phenylenediamine moiety increase the activation energy required for ROP. The more rigid aromatic structure restricts molecular mobility, thereby elevating the polymerization temperature compared with the more flexible ethylenediamine (EDA) linker in **IBZ-EDA**.[32,52] The intensity of this exotherm decreased with increasing temperature and fully disappeared above 200 °C, confirming complete crosslinking. This finding is further supported by the FTIR spectra (Fig. 5b), in which the characteristic benzoxazine absorption bands (*e.g.*, the bands at about 923 and 1228 cm^{-1}) disappear after curing, while a broad O—H stretching band emerges at approximately 3200 cm^{-1}. These changes confirmed the successful ROP and formation of the cross-linked **Poly(IBZ–PHDA)** network.

To quantitatively evaluate the polymerization progress, the degree of conversion at each pre-curing temperature was determined by integrating the residual curing enthalpy from the DSC thermograms using the uncured monomer as the reference (0% conversion). For **IBZ-EDA**, the conversion reached 42.1% at 100 °C, 87.7% at 150 °C, and 100% at 200 °C. For **IBZ-PHDA**, the conversion was 7.1% at 100 °C, 28.6% at 150 °C, 73.8% at 200 °C, and 100% at 250 °C. These results confirmed that complete polymerization was achieved at 200 °C for **IBZ-EDA** and at 250 °C for **IBZ-PHDA**.

The conversion was further verified by quantitative FTIR analysis, in which the characteristic benzoxazine band at about 1230 cm^{-1} (C—O—C asymmetric stretching) was normalized against the imide C=O band at about 1720 cm^{-1} as an internal reference. For **IBZ-EDA**, FTIR-derived conversion values were 40.5% at 100 °C, 85.2% at 150 °C, and 100% at 200 °C. For **IBZ-PHDA**, the conversion was 6.8% at 100 °C, 26.5% at 150 °C, 71.2% at 200 °C, and 100% at 250 °C. The FTIR-derived conversion values were in excellent agreement with the DSC results, confirming the reliability of both methods and providing strong quantitative evidence for complete polymerization upon completion of the respective curing protocols.

Thermal Stability of IBZ-EDA and IBZ-PHDA at Elevated Temperatures

The thermal degradation behaviors of **IBZ-EDA** and **IBZ-PHDA** were investigated by TGA under a nitrogen atmosphere. Figs. 6(a) and 6(b) show the TGA curves of **IBZ-EDA** and **IBZ-PHDA**, respectively, after thermal curing at various temperatures (25, 100, 150, 200, and 250 °C).

As shown in Fig. 6(a), the **IBZ-EDA** samples exhibited a pro-

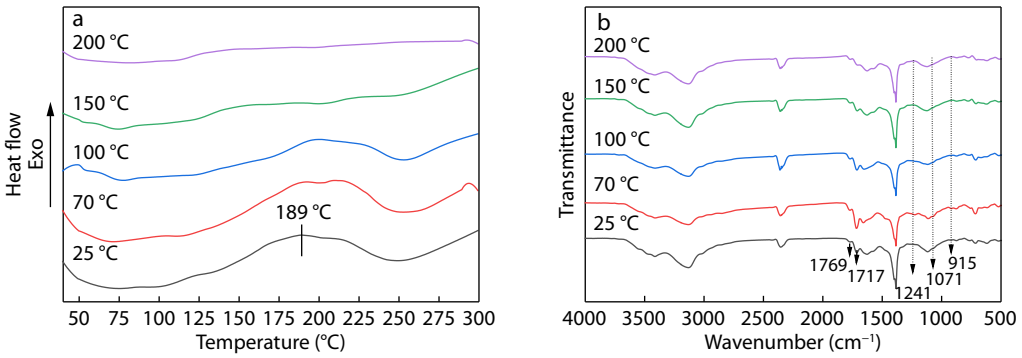

Fig. 4 Polymerization behavior of **IBZ-EDA** investigated by (a) DSC and (b) FTIR at different temperatures.

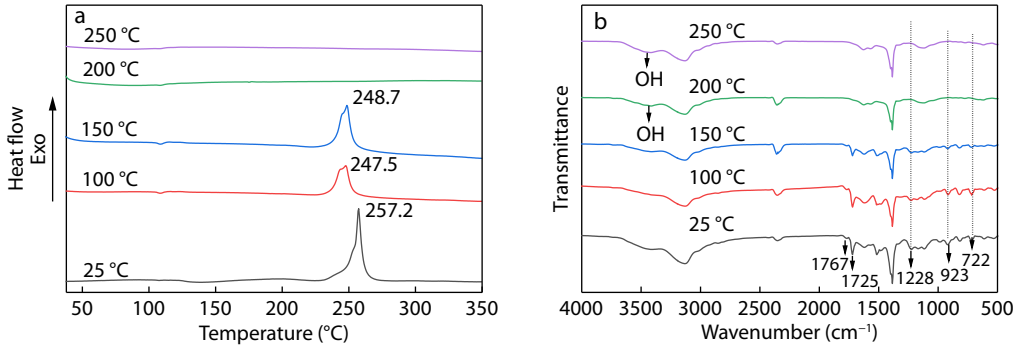

Fig. 5 Polymerization behavior of **IBZ-PHDA** investigated by (a) DSC and (b) FTIR at different temperatures.

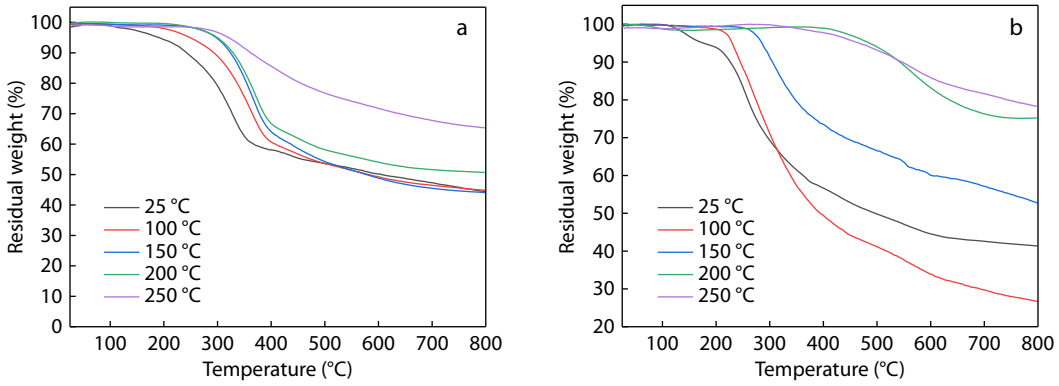

Fig. 6 Thermal degradation behavior investigated by TGA for (a) **IBZ-EDA** and (b) **IBZ-PHDA** at different temperatures.

gressive shift in the weight-loss profiles toward higher temperatures with increasing curing temperature, indicating enhanced thermal stability. The uncured sample (25 °C) begins to decompose at a relatively low temperature, whereas samples cured at elevated temperatures show delayed degradation, attributed to the formation of a more extensively crosslinked and thermally stable polymeric network.[53]

Similarly, the **IBZ-PHDA** system (Fig. 6b) displayed the same trend, but with an overall higher thermal stability compared to **IBZ-EDA**. samples cured at 200 and 250 °C degraded at considerably higher temperatures, and their residual char yields at 800 °C increased accordingly, reflecting the greater rigidity and aromatic content of the *para*-phenylenediamine-based structure.

This behavior confirms that the thermal treatment promotes further polymerization and ring formation, resulting in a denser and more compact network with enhanced resistance to thermal decomposition. The superior thermal stability of the **IBZ-PHDA** system is attributed to its aromatic diamine structure, which imparts greater rigidity and thermal resistance than the aliphatic diamine in **IBZ-EDA**. This observation aligns with previous reports, indicating that aromatic diamine-based benzoxazines yield polymers with high thermal stability and char yields, whereas chain ends, which are more prevalent in aliphatic systems, serve as initiation sites for thermal degradation.[53]

Tables 1 and 2 summarize the key thermal parameters derived from the TGA data for the **IBZ-EDA** and **IBZ-PHDA** systems at various curing temperatures. These parameters include the temperatures corresponding to 5% and 10% weight loss (T_5 and T_{10}), the char yield at 800 °C, and the calculated limiting oxygen index (LOI) values. Flame-retardant performance was evaluated using the char yield at 800 °C, and the LOI was calculated according to the Van Krevelen–Hoftyzer equation.[54]

Table 1 Thermal parameters derived from TGA thermograms of **IBZ-EDA**.

Temperature (°C)	T_{d5} (°C)	T_{d10} (°C)	CY	LOI (%)
Uncured	191	241	44	35.1
100	248	293	45	35.5
150	296	324	44	35.1
200	300	327	51	37.9
250	380	417	65	43.1

T_{d5} and T_{d10} represent the temperatures at which 5% and 10% weight loss occur, respectively. The char yield (CY) was measured at 800 °C, while the limiting oxygen index (LOI) was calculated according to this equation: LOI = 17.5 + 0.4(CY).

Table 2 Thermal parameters derived from TGA thermograms of **IBZ-PHDA**.

Temperature (°C)	T_{d5} (°C)	T_{d10} (°C)	CY	LOI (%)
Uncured	160	222	41	33.9
100	215	235	27	27.9
150	275	298	53	38.2
200	464	531	75	47.1
250	489	559	79	49.1

T_{d5} and T_{d10} represent the temperatures at which 5% and 10% weight loss occur, respectively. The char yield (CY) was measured at 800 °C, while the Limiting Oxygen Index (LOI) was calculated according to this equation: LOI = 17.5 + 0.4(CY).

$$\mathrm{LOI} = 17.5 + 0.4\,(\mathrm{CY}) \quad (1)$$

For the **IBZ-EDA** system, both T_5 and T_{10} increase progressively from 191 and 241 °C for the uncured sample to 380 and 417 °C for the sample cured at 250 °C, respectively. The char yield also increased from 44% to 65%, corresponding to an improvement in LOI from 35.1% to 43.1%. These results demonstrate a clear enhancement in both thermal stability and flame resistance as the curing temperature increased. These findings are consistent with recent studies reporting that high char yields in PBZ systems are correlated with outstanding thermal stability and excellent flame retardancy, including the V-0 classification.[55]

In the case of **IBZ-PHDA**, this improvement was even more pronounced. The T_5 and T_{10} values increase from 160 and 222 °C for the uncured sample to 489 and 559 °C after curing at 250 °C. Similarly, the char yield reached 79% at 250 °C, corresponding to an LOI value of 49.1%. These results demonstrate that **IBZ-PHDA** exhibits superior thermal and flame-retardant properties compared with **IBZ-EDA**, which is attributed to its more rigid aromatic structure and the formation of a highly crosslinked polymeric network upon curing. These values are notably higher than those reported for conventional PBZs, which typically exhibit T_{10} values in the range of 400–450 °C and char yields of 50%–60% at 800 °C.[56–58] The aromatic core structure contributes to a more compact and thermally stable network, thereby enhancing resistance to thermal degradation.[58]

Examination of the TGA profiles revealed that both polymers underwent a multi-stage degradation process. The first degradation stage, occurring in the range of 300–450 °C for **Poly(IBZ-EDA)** and 450–550 °C for **Poly(IBZ-PHDA)**, was attributed to the decomposition of the Mannich bridges and cleavage of the less stable aliphatic or aromatic linkages within the polybenzoxazine network. The second degradation stage, occurring in the range of 450–600 °C for **Poly(IBZ-EDA)** and 550–700 °C for **Poly(IBZ-PHDA)**, corresponds to the degradation of the thermally robust imide and aromatic moieties, which are responsible for the high char yields observed. The higher degradation temperatures and greater char-forming ability of **Poly(IBZ-PHDA)** were attributed to its higher aromatic content and greater crosslink density, which enhanced the thermal stability of the material.

The remarkably high LOI value of 49.1% achieved in this study was primarily attributed to the incorporation of imide and aromatic moieties within the benzoxazine framework. These rigid, thermally stable units significantly enhanced the thermal stability and char-forming ability of the material. This finding aligns with recent studies on nitrogen-containing heterocyclic PBZ systems, in which imidazole-core structures demonstrated enhanced flame retardancy, achieving char yields of 65% and LOI values of 49.1% by forming protective char layers during combustion.[59]

It is noteworthy, the char yield of IBZ-PHDA after treatment at 100 °C (26%) was lower than that of the uncured sample (41%). This anomaly arises from partial curing at this temperature, at which the benzoxazine rings are only minimally opened (7.1% conversion, as determined by DSC). The Thermal treatment at 100 °C is sufficient to volatilize residual solvent, unreacted monomers, and low-molecular-weight species that have not yet been incorporated into the crosslinked network, resulting in a transient reduction in residual char upon pyrolysis. As the curing temperature increased to 150 °C and beyond, the degree of crosslinking improved substantially, resulting in a significant enhancement of char yield (51% at 150 °C, 74% at 200 °C, and 79% at 250 °C). This behavior confirms that the thermal stability improves continuously with increasing curing temperature once a sufficient degree of network formation has been achieved.

The exceptionally high T_{d10} (559 °C) and LOI (49.1%) values exhibited by **Poly(IBZ-PHDA)** warrant a detailed analysis of the structural features contributing to this outstanding performance. This exceptional performance arises from a synergistic combination of several structural features. (i) High imide density: the presence of two phthalimide groups per repeating unit provides multiple thermally stable segments that resist degradation and promote char formation upon pyrolysis. (ii) High aromatic content: the rigid *para*-phenylene linker introduced an additional aromatic ring, increasing the total aromatic carbon content to 30 atoms per repeating unit. The high aromaticity enhances the thermal stability through strong C—C and C—N bonds and promotes the formation of graphitic-like char structures during decomposition. (iii) Rigid crosslinked network topology: the difunctional, rigid monomer structure promotes the formation of a densely crosslinked three-dimensional network with restricted molecular mobility and reduced concentration of chain ends, which are known initiation sites for thermal degradation. (iv) Enhanced hydrogen bonding: *ortho*-phthalimide substitution facilitates the formation of intramolecular hydrogen bonds between phenolic and OH groups and imide carbonyl oxygen atoms, creating a six-membered hydrogen-bonded ring that further stabilizes the network.

The quantitative comparison between **Poly(IBZ-PHDA)** and **Poly(IBZ-EDA)**, which shares the same phthalimide and benzoxazine units but contains a flexible aliphatic ethylenediamine linker, reveals that the replacement of the flexible aliphatic linker with the rigid aromatic PHDA linker improves T_{d10} by 142 °C, char yield by 14%, and LOI by 6%. This comparison underscores the critical role of aromaticity and network rigidity in determining the thermal stability and flame retardancy.

XRD Investigation of Structural Ordering

XRD analysis was performed to investigate the structural characteristics and ordering of the synthesized monomers and their corresponding polymers. As shown in Fig. 7(a), the XRD patterns of both monomers (**IBZ-EDA** and **IBZ-PHDA**) displayed several distinct, relatively sharp diffraction peaks in the 2θ range of approximately 10°–30°, indicating a significant degree of crystalline order in the monomeric state. These sharp reflections are attributed to the ordered molecular arrangement and strong intermolecular interactions, including π–π stacking between the aromatic phthalimide and benzoxazine rings, and intermolecular hydrogen bonding,[60] which promote efficient molecular packing prior to polymerization. The presence of multiple sharp peaks suggests a well-defined crystal lattice with

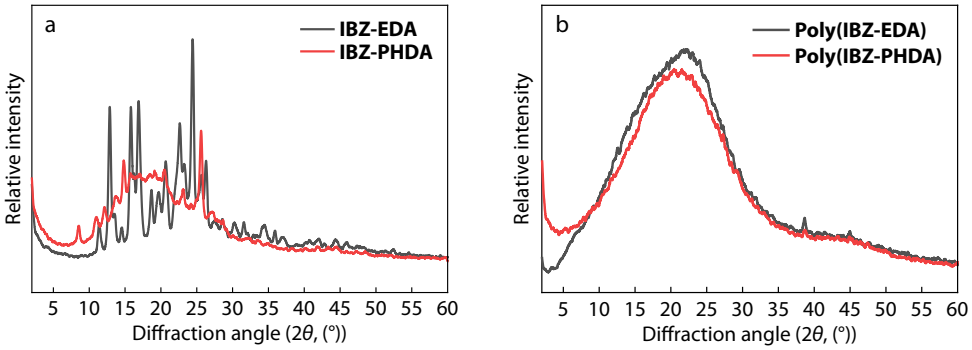

Fig. 7 XRD patterns of (a) the synthesized monomers **IBZ-EDA** and **IBZ-PHDA** and (b) the corresponding cured polymers **Poly(IBZ-EDA)** and **Poly(IBZ-PHDA)**.

https://doi.org/10.1007/s10118-026-3833-0

specific intermolecular distances (*d*-spacings), which is consistent with the high purity of the monomers, as confirmed by elemental analysis and NMR.

Following thermal curing and ring-opening polymerization, the XRD patterns of the resulting polymers, **Poly(IBZ-EDA)** and **Poly(IBZ-PHDA)**, exhibited profound transformations (Fig. 7b). Both polymers displayed a broad diffraction halo centered at approximately 2θ of 18°–25°, which is characteristic of amorphous polymeric materials.[61] The disappearance of the sharp reflections observed in the monomer patterns and the emergence of a broad halo confirmed the loss of long-range crystalline order upon network formation. This transition from a crystalline monomer to an amorphous polymer is typical of crosslinked thermosetting systems, and arises from the disruption of ordered molecular packing during ring-opening polymerization. Random crosslinking, restricted chain mobility, and three-dimensional network topology prevent polymer chains from reordering into crystalline domains.

Although both polymers were predominantly amorphous, subtle differences were observed between them. **Poly(IBZ-EDA)** exhibited a slightly broader halo, suggesting a more uniform distribution of intermolecular distances within the amorphous network. In contrast, the halo for **Poly(IBZ-PHDA)** was slightly narrower, and the background scattering was somewhat higher, which may indicate the persistence of a slightly higher degree of local ordering owing to the rigid para-phenylene linker and higher aromatic content. The rigid, rod-like nature of the *para*-phenylene linker promotes stronger π–π stacking interactions and more efficient local packing of the aromatic units, even within the amorphous network.[53] Nevertheless, the absence of sharp diffraction peaks confirms that the local ordering does not extend to long-range crystalline domains.[62]

These XRD results are consistent with the thermal properties of the polymers. The amorphous, highly crosslinked nature of the networks contributes to their exceptional thermal stability by restricting chain mobility and evenly distributing thermal stress throughout the network.[63] The lack of long-range crystalline order, combined with the high crosslink density, explains the remarkable T_{d10} values and high char yields observed for both polymers, particularly **Poly(IBZ-PHDA)**.

Microstructural Morphology of Poly(IBZ-EDA) and Poly(IBZ-PHDA)

The surface and fracture morphologies of the cured imide-functionalized PBZs, **Poly(IBZ-EDA)** and **Poly(IBZ-PHDA)**, were investigated by SEM, as shown in Fig. 8. Prior to SEM observation, the coated samples were dried under ambient conditions, mounted on aluminum stubs using conductive carbon tape, and sputter-coated with a thin platinum layer to improve the surface conductivity and minimize charging effects during imaging. SEM micrographs reveal brittle fracture characteristics typical of highly crosslinked thermosetting polymers.[64,65]

Both materials exhibited dense layered lamellar structures with parallel ridge-like and periodic wrinkle patterns. The observed wrinkle morphology was attributed to the shrinkage and stress-relaxation processes occurring during solvent evaporation and film formation. As the coating layer contracts during drying and curing, a mismatch between the dimensional changes of the polymer coating and the underlying substrate generates compressive stresses, which are relieved by the formation of wrinkle-like surface features. Similar morphologies have been reported for PB-based and hybrid thermosetting coating systems. **Poly(IBZ-EDA)** exhibited a relatively smooth, compact morphology with uniform fracture planes and minimal microvoids, suggesting homogeneous crosslinking and robust network integrity. The dense and continuous surface further indicates efficient chain pack-

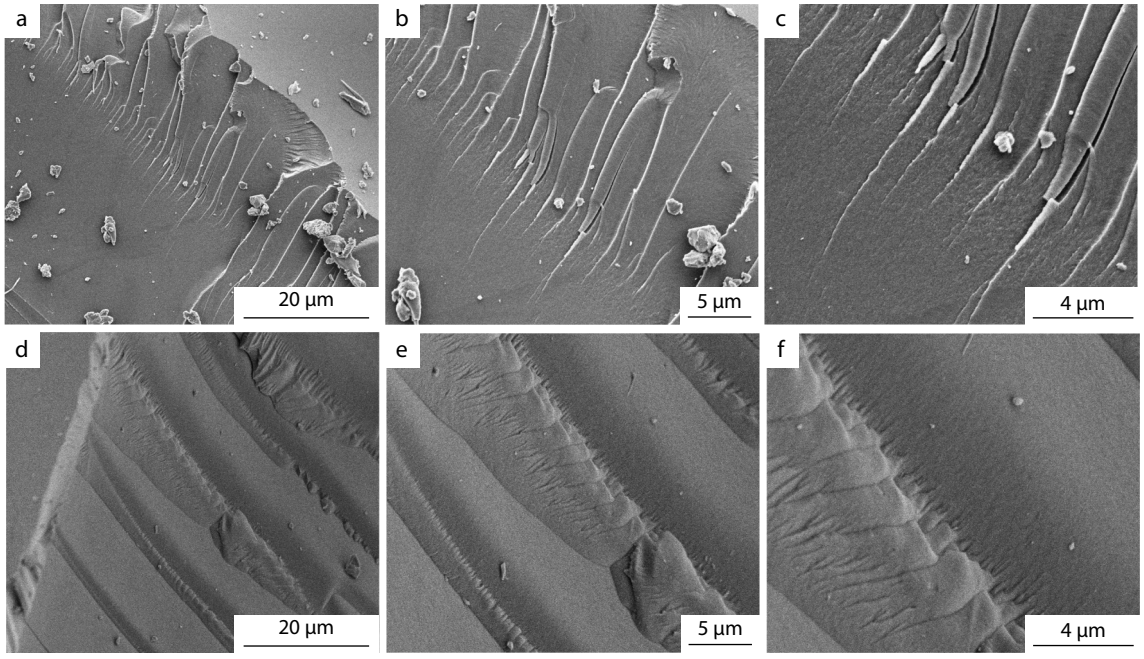

Fig. 8 SEM images showing the surface morphology of (a–c) **Poly(IBZ-EDA)** and (d–f) **Poly(IBZ-PHDA)** at different magnifications.

ing and strong intermolecular interactions, which restrict chain mobility and contribute to the enhanced thermal stability.[66] In contrast, **Poly(IBZ-PHDA)** exhibits a rougher fracture surface with visible microcracks and localized debris. This morphology is attributed to the higher rigidity and aromatic nature of the PHDA segment, which increases the internal stress during curing and cooling, thereby promoting a more pronounced brittle fracture behavior. The increased backbone rigidity also facilitates stress concentration, resulting in microstructural irregularities.[67] Overall, SEM observations confirmed the formation of densely crosslinked imide–benzoxazine thermoset networks. The morphological differences between the two polymers arise primarily from the structural characteristics of the diamine segment, which influence chain packing, network rigidity, stress development, and ultimately, the thermal and mechanical performance of the resulting PBZ materials.

The SEM micrographs revealed distinct morphological differences between the two polymers, arising from the fundamentally different molecular architectures of the bridging units. **Poly(IBZ-EDA)**, bearing a flexible ethylenediamine linker, exhibited a relatively smooth, compact, and uniform surface with homogeneous fracture planes and minimal microvoids. This morphology suggests efficient chain packing and strong intermolecular interactions, which restrict chain mobility and contribute to the enhanced thermal stability. The flexible aliphatic linker allows greater molecular mobility during curing, facilitating stress relaxation and reducing the buildup of internal stresses, which would otherwise lead to surface irregularities.

In contrast, **Poly(IBZ-PHDA)** bearing a rigid *para*-phenylene linker exhibited a denser but rougher fracture surface with visible microcracks and localized debris. This morphology is attributed to the greater rigidity and aromatic nature of the PHDA segment, which increases the internal stress during curing and cooling, thereby promoting more pronounced brittle fracture behavior. The increased backbone rigidity also facilitated stress concentration, resulting in microstructural irregularities.

The denser surface observed for **Poly(IBZ-PHDA)** arises from several interrelated factors. First, the rigid *para*-phenylene linker promoted the formation of a more densely crosslinked network, as evidenced by the significantly higher char yield (79% versus 64%) and thermal stability (T_{d10} of 559 °C versus 417 °C) of **Poly(IBZ-PHDA)** compared to **Poly(IBZ-EDA)**. Second, the high aromatic content facilitates π–π stacking interactions and extensive hydrogen bonding between the phenolic and OH groups and imide carbonyl oxygen atoms, tertiary amine nitrogen atoms, and ether oxygen atoms. These intermolecular interactions act as physical crosslinks that pull the polymer chains into closer proximity, increasing the overall packing density. Third, the restricted chain mobility imposed by the rigid aromatic linker reduced the free volume within the polymer matrix, resulting in a more compact and tightly packed network. In contrast, the flexible ethylenediamine linker in **Poly(IBZ-EDA)** allows greater chain mobility and conformational freedom, increasing the free volume and reducing the packing efficiency, which manifests as a less dense but smoother surface morphology.

Photophysical Properties

*UV-visible absorption and excitation spectral properties of **IBZ-EDA** and **IBZ-PHDA** in DMF solution*

The electronic absorption properties of **IBZ-EDA** and **IBZ-PHDA** were investigated in DMF at concentrations ranging from 10^{-6} mol/L to 10^{-4} mol/L, and the corresponding spectra are presented in Figs. 9(a) and 9(b). Both monomers exhibit two characteristic absorption bands centered at approximately 260 and 283 nm, indicating that the fundamental electronic transitions are governed by similar chromophoric units despite the different bridging groups connecting the benzoxazine moieties. The observed absorption features were primarily attributed to $\pi \rightarrow \pi^*$ transitions within the aromatic benzoxazine and phthalimide segments, with possible contributions from the $n \rightarrow \pi^*$ transitions associated with the carbonyl groups of the imide functionalities. The coexistence of electron-rich benzoxazine rings and electron-deficient phthalimide units creates a molecular framework that supports localized excited states and partial intramolecular charge redistribution upon photoexcitation.

For **IBZ-EDA**, the absorption intensity increases systematically with concentration, reaching absorbance values of approximately 2.2 and 1.3 at 283 and 260 nm, respectively, at 10^{-4} mol/L. At 10^{-5} mol/L, these values decrease to approximately 1.0 and 0.6, while further dilution to 10^{-6} mol/L results in absorbances of about 0.12 and 0.15. A similar concentration-dependent trend was observed for **IBZ-PHDA**, although the relative intensity distribution of the two absorption bands differed slightly. At 10^{-4} mol/L, absorbance values of approximately 1.3 and 1.2 are observed at 283 and 260 nm, respectively, decreasing to 0.9 and 0.6 at 10^{-5} mol/L and to 0.6 and 0.4 at 10^{-6} mol/L. Importantly, neither monomer exhibits appreciable absorption above approximately 325 nm, indicating that the lowest-energy electronic transitions remain confined to the ultraviolet region and that any visible emission observed in subsequent fluorescence measurements may originate from relaxation processes occurring after excitation into these higher-energy electronic states.

Although both compounds possess identical terminal phthalimide substituents and benzoxazine units, subtle differences in their absorption profiles can be rationalized by the nature of the bridging linkers. In **IBZ-EDA**, the flexible ethylene spacer electronically isolates the two benzoxazine-phthalimide segments to a greater extent, resulting in transitions that are predominantly localized within individual aromatic subunits. In contrast, **IBZ-PHDA** contains a rigid paraphenylene bridge that increases molecular rigidity and enhances through-bond electronic communication between aromatic fragments. The resulting increase in the electronic delocalization can alter the transition probabilities and oscillator strengths, accounting for the observed differences in the absorption intensity and band distribution between the two monomers.

To assess the linearity of the concentration-dependent absorbance, molar absorptivity values were calculated at both absorption maxima across the investigated concentration range. For **IBZ-EDA**, the molar absorptivity at 283 nm decreased from 1.20×10^5 L/(mol·cm) at 10^{-6} mol/L to 1.00×10^5 L/(mol·cm) at 10^{-5} mol/L and further to 2.20×10^4 L/(mol·cm)

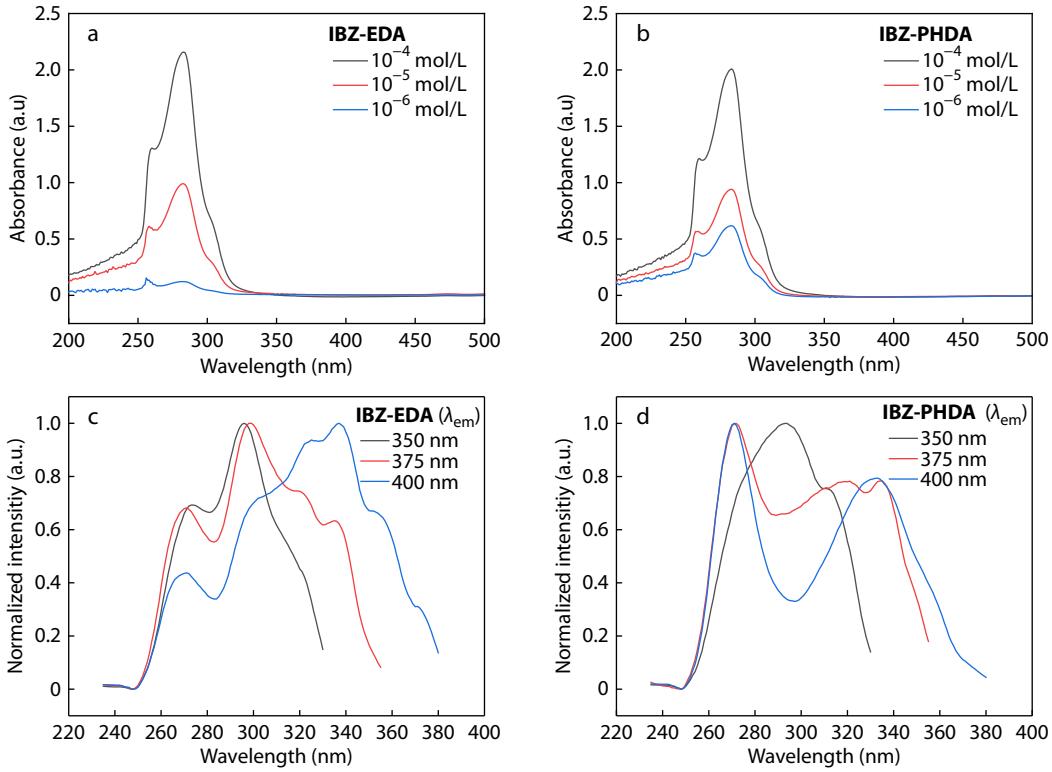

Fig. 9 (a) UV-Vis absorption spectra of **IBZ-EDA** in DMF solution at concentrations of 10^{-4}, 10^{-5}, and 10^{-6} mol/L; (b) UV-Vis absorption spectra of **IBZ-PHDA** in DMF solution at the same concentration range; (c) Excitation spectra of **IBZ-EDA** (10^{-5} mol/L in DMF) recorded at emission wavelengths (λ_{em}) of 350, 375, and 400 nm; (d) Excitation spectra of **IBZ-PHDA** (10^{-5} mol/L in DMF) under the same emission conditions.

at 10^{-4} mol/L, indicating deviations from the Beer-Lambert law at higher concentrations. A similar trend was observed for **IBZ-PHDA**, where the molar absorptivity at 283 nm decreased from 6.00×10^5 L/(mol·cm) at 10^{-6} mol/L to 9.00×10^4 L/(mol·cm) at 10^{-5} mol/L and 1.30×10^4 L/(mol·cm) at 10^{-4} mol/L. These deviations are primarily attributed to inner filter effects and ground-state aggregation at higher concentrations, where the elevated absorbance values (A>2.0) and increased molecular proximity promote intermolecular interactions that alter electronic transition probabilities. Importantly, the photoluminescence measurements were predominantly conducted at 10^{-5} and 10^{-6} mol/L, where the absorbance remains within a more reliable range, ensuring that the observed emission behavior reflects the intrinsic properties of the monomers.

To obtain further insight into the emissive states populated after photoexcitation, excitation spectra were recorded for both monomers at an intermediate concentration of 10^{-5} mol/L while monitoring emission at 350, 375, and 400 nm (Figs. 9c and 9d). In both systems, the excitation spectra differed significantly from the corresponding absorption spectra and exhibited multiple peaks and shoulders distributed throughout the 250–300 nm region. Nevertheless, all excitation profiles consistently exhibit prominent features in the 260–270 nm and 280–290 nm ranges, which coincide with the principal absorption bands observed in the UV-visible spectra. This correspondence confirms that excitation into these electronic transitions directly contributes to the formation of the emissive excited states.

A notable feature of excitation measurements is the pronounced dependence of the spectral shape on the monitored emission wavelength. The relative intensities of the individual excitation bands change substantially as the emission wavelength is shifted from 350 nm to 400 nm, and the enhanced contributions from longer-wavelength excitation components become increasingly evident at higher emission wavelengths. This behavior indicates that the fluorescence does not originate from a single homogeneous excited-state population. Instead, the results suggest the presence of multiple emissive species or excited-state conformations possessing distinct excitation-emission relationships. This phenomenon is commonly associated with heterogeneous excited-state distributions, conformational diversity, or coexistence of locally excited and charge-transfer-like states within complex aromatic systems.

The deviation between the absorption and excitation spectral profiles provides additional evidence that the excited-state dynamics of these monomers are more complex than those expected for simple molecular fluorophores. If the emission originated from a single emissive center, the excitation spectra would closely resemble the absorption spectra regardless of the monitored emission wavelength. Therefore, the observed wavelength-dependent excitation behavior suggests a selective population of different emissive states, depending on the excitation energy and detection wavelength. Considering the molecular structures of **IBZ-EDA** and **IBZ-PHDA**, this behavior may arise from variations in the electronic coupling between the benzoxazine, phthalimide, and

https://doi.org/10.1007/s10118-026-3833-0

bridging units, leading to multiple relaxation pathways and distinct emissive environments in solution.

Although the absorption spectra show negligible absorbance above 325 nm, there is weak absorption, although it is not readily visible in the conventional spectra, owing to its low oscillator strength, which is consistent with the existence of low-probability electronic transitions or vibrationally hot transitions that can be populated upon excitation at longer wavelengths. The excitation spectra (Figs. 9c and 9d) provide further evidence for these weak absorption states, as the emission monitored at longer wavelengths (*e.g.*, 400 nm) exhibited contributions from the excitation components in the 280–290 nm region and showed a tail extending toward longer wavelengths. These observations confirmed that the emission observed upon excitation at 350, 375, and 400 nm may arise from the genuine, albeit weak, absorptive states of the monomers.

Furthermore, the stronger wavelength dependence observed in the excitation spectra implies that structural flexibility and local molecular organization may influence the excited-state evolution, even in dilute solutions. The presence of several heteroatom-rich functionalities, including imide carbonyl groups, tertiary amine centers, and ether linkages, facilitates the formation of different excited-state configurations through intramolecular electronic interactions. Consequently, the photoluminescence of these monomers is expected to exhibit excitation-dependent characteristics, which will be further examined through the emission studies presented in the following section.

Notably, the PL measurements used for the excitation-dependent emission analysis were conducted predominantly at 10^{-5} mol/L, where the absorbance at the excitation wavelengths (350, 375, and 400 nm) was negligible. Under these conditions, the inner filter effects and reabsorption did not significantly affect the PL measurements. For the PL measurements at 10^{-4} mol/L, a triangular (front-face) fluorescence cell was employed to minimize inner-filter effects and reabsorption. High-concentration measurements were included to demonstrate concentration-dependent spectral evolution, but quantitative interpretation of these data should consider potential inner-filter effects.

The variation in molar absorptivity with concentration may arise from a combination of factors, including inner-filter effects at high absorbance values, molecular aggregation through π–π stacking interactions, and instrumental limitations at absorbance values exceeding 2.0. Although aggregation is a plausible explanation for the observed changes, further experimental evidence is required to definitively confirm the presence of aggregates.

Photoluminescence properties of the monomers in DMF solution

The fluorescence behavior of **IBZ-EDA** and **IBZ-PHDA** was investigated in DMF through concentration-dependent and excitation-dependent emission measurements, and the results are summarized in Fig. 10. The emission characteristics revealed a pronounced dependence on both the molecular concentration and the excitation wavelength, indicating the coexistence of multiple emissive states arising from the complex electronic structures of these imide-functional benzoxazine monomers.

The concentration-dependent emission spectra of **IBZ-EDA** recorded at λ_{ex}=350 nm (Fig. 10a) exhibit notable spectral evolution as the concentration increases from 10^{-6} mol/L to 10^{-4} mol/L. At the lowest concentration (10^{-6} mol/L), the emission was dominated by a broad band extending from approximately 370 nm to 500 nm, with a principal maximum located at 412 nm, accompanied by two additional peaks at 393 and 435 nm of comparable intensity. The presence of several closely spaced emission maxima suggests the existence of multiple radiative relaxation pathways originating from the distinct excited-state configurations. Upon increasing the concentration to 10^{-5} mol/L, the same principal emission maximum at 412 nm was retained; however, the features at 393 and 435 nm evolved into less pronounced shoulders, indicating increased electronic communication among the molecular species in solution. Simultaneously, a second broad emission band emerged within the 500–600 nm region. Further increasing the concentration to 10^{-4} mol/L results in a more simplified short-wavelength emission profile dominated by the 412 nm band with a weaker secondary peak around 425 nm, while the long-wavelength emission component becomes substantially more intense. The progressive enhancement of the longer-wavelength emission with increasing concentration strongly suggests the formation of emissive associated species, likely arising from intermolecular interactions involving aromatic benzoxazine and phthalimide units. This behavior is consistent with the generation of aggregated excited states, excimer-like species, or cluster-induced emissive domains, which become increasingly populated at higher concentrations.

A similar concentration-dependent trend was observed for **IBZ-PHDA** (Fig. 10b), although notable differences were observed because of the more rigid *para*-phenylene bridge connecting the benzoxazine units. At 10^{-4} mol/L, **IBZ-PHDA** exhibits a distinct dual-emission profile consisting of a short-wavelength band centered near 412 nm and a second broad emission centered at approximately 550 nm. The appearance of a well-developed long-wavelength band indicates efficient formation of lower-energy emissive states at elevated concentrations. In contrast, the spectra recorded at 10^{-5} and 10^{-6} mol/L are characterized primarily by two emission maxima at approximately 393 and 412 nm together with a broad tail extending toward longer wavelengths. Although this long-wavelength tail was present at both concentrations, its intensity was significantly greater at 10^{-5} mol/L than at 10^{-6} mol/L, again indicating a concentration-dependent contribution from intermolecularly generated emissive species.

The emergence and growth of longer-wavelength emission components in both monomers suggest that fluorescence is not exclusively governed by isolated molecular excited states. The molecular structures contain multiple electron-rich and electron-deficient functionalities, including benzoxazine nitrogen atoms, ether oxygen atoms, and imide carbonyl groups, which can participate in through-space electronic interactions, even in solution. As the molecular proximity increases with concentration, these interactions may facilitate the formation of stabilized excited states possessing lower transition energies than the locally excited states responsible for the blue emission region. Therefore, the stronger de-

https://doi.org/10.1007/s10118-026-3833-0

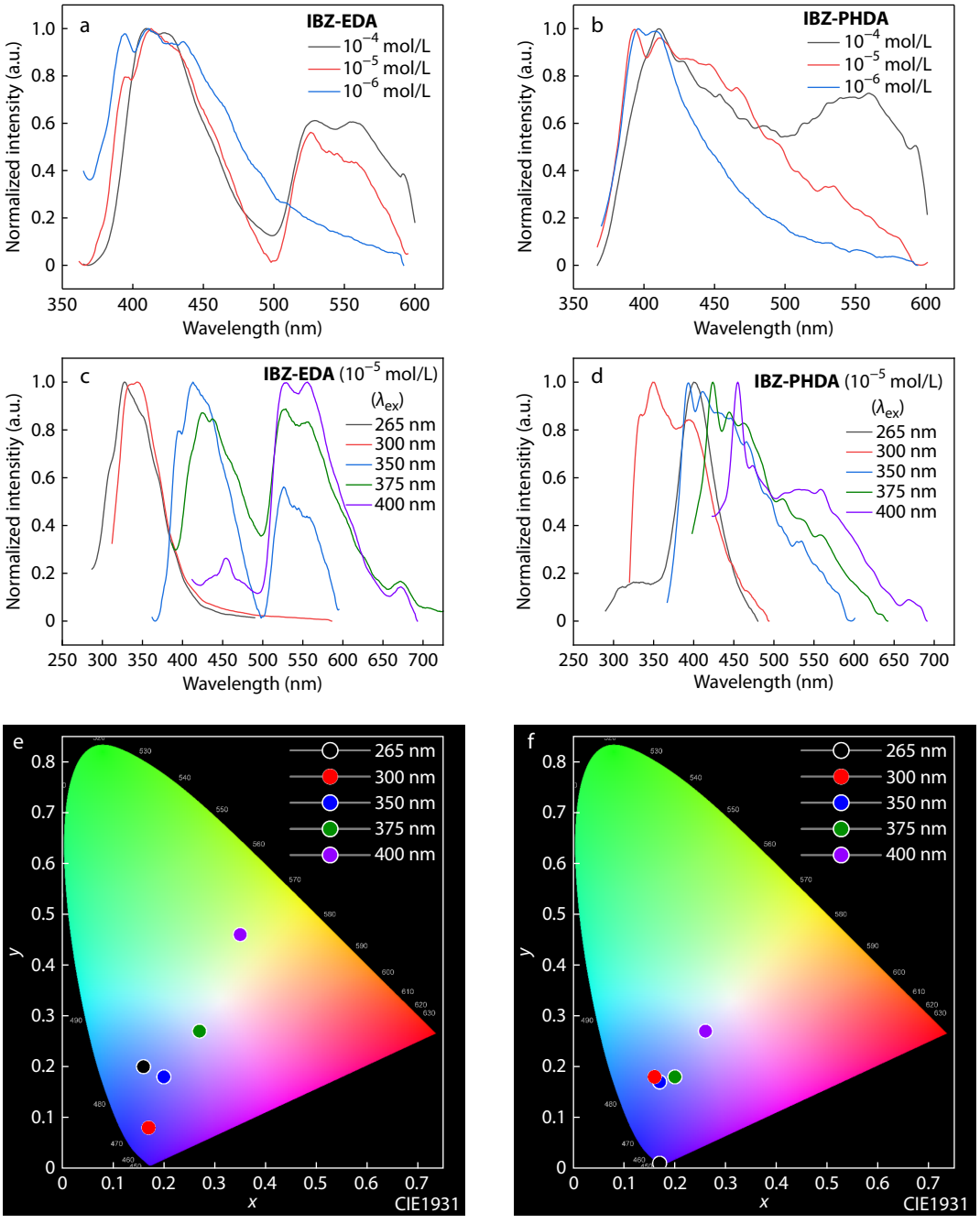

Fig. 10 (a) Emission spectra of **IBZ-EDA** in DMF at concentrations of 10^{-4}, 10^{-5}, and 10^{-6} mol/L recorded at λ_{ex}=350 nm; (b) Emission spectra of **IBZ-PHDA** in DMF at concentrations of 10^{-4}, 10^{-5}, and 10^{-6} mol/L recorded at λ_{ex}=350 nm; (c) Excitation-dependent emission spectra of **IBZ-EDA** (10^{-5} mol/L in DMF) measured at λ_{ex} of 265, 300, 350, 375, and 400 nm; (d) Excitation-dependent emission spectra of **IBZ-PHDA** (10^{-5} mol/L in DMF) measured at λ_{ex} of 265, 300, 350, 375, and 400 nm; (e) Corresponding CIE chromaticity coordinates of **IBZ-EDA** derived from the spectra shown in Fig. 10(c) and (f) corresponding CIE chromaticity coordinates of **IBZ-PHDA** derived from the spectra shown in Fig. 10(d).

velopment of the long-wavelength band in concentrated solutions provides compelling evidence for aggregation-assisted excited-state relaxation.

This excitation-dependent emission behavior further supports the existence of multiple emissive centers. As shown in Fig. 10(c), the emission spectra of **IBZ-EDA** (10 mol/L) underwent significant changes upon varying the excitation wavelength from 265 nm to 400 nm. Excitation at 265 and 300 nm produces relatively similar emission profiles dominated by a single short-wavelength emission band, indicating a preferential population of higher-energy locally excited states. However, excitations at 350, 375, and 400 nm led to the appearance of dual-emission characteristics, accompanied by a progressive increase in the intensity of the long-wavelength region. The systematic enhancement of the lower-energy emission component with increasing excitation wavelength demonstrates the selective excitation of emissive states that are not efficiently populated under higher-energy excitation

conditions.

An even more pronounced excitation-wavelength dependence was observed for **IBZ-PHDA** (Fig. 10d). Unlike **IBZ-EDA**, the emission profiles of **IBZ-PHDA** displayed distinct spectral shapes at each excitation wavelength, indicating a higher degree of excited-state heterogeneity. As the excitation wavelength increased, the contribution of the long-wavelength emission region became progressively more significant, which is consistent with the preferential population of lower-energy emissive states. The rigid para-phenylene linker in **IBZ-PHDA** likely promotes more efficient electronic communication between the two benzoxazine-phthalimide units, resulting in a broader distribution of excited-state configurations, and consequently, stronger excitation-dependent fluorescence behavior.

The flexible linker in **IBZ-EDA** and the rigid aromatic bridge in **IBZ-PHDA** created different distributions of conformational and electronic states, contributing to the observed differences in spectral evolution. The strong excitation dependence, together with the non-superimposable excitation spectra discussed previously, confirms that the fluorescence in these systems may arise from multiple emissive species rather than a single homogeneous excited-state population.

The excitation-dependent emission observed for both monomers is consistent with the coexistence of locally excited (LE) states and more delocalized excited states that may possess partial charge transfer characteristics. The phthalimide groups acted as strong electron acceptors, whereas the benzoxazine framework contained electron-rich donor sites. Therefore, photoexcitation may generate excited states with varying degrees of charge separation depending on the excitation energy and molecular conformation. However, it should be noted that the definitive assignment of the specific electronic nature of these states (*e.g.*, intramolecular charge transfer (ICT) versus excimer-like versus aggregate-associated) cannot be unambiguously determined from steady-state PL measurements alone. Therefore, the proposed assignments are presented as plausible interpretations that are consistent with the available data, rather than as definitive conclusions. Additional spectroscopic techniques, including time-resolved photoluminescence, solvent-polarity-dependent emission, and temperature-dependent measurements, are required for more rigorous mechanistic assignment.

The PL spectra in Figs. 10(a) and 10(b) are presented in a normalized form to facilitate the comparison of spectral shapes. The actual emission intensities (in arbitrary units) increased with increasing concentration, consistent with the presence of concentration-dependent emissive species. However, it should be noted that normalized spectra do not allow for the quantitative determination of relative quantum yields. Absolute or relative PL quantum yield measurements are required to assess whether the emission efficiency increases upon polymerization or with changes in the concentration.

The corresponding CIE chromaticity coordinates derived from the excitation-dependent emission spectra are presented in Figs. 10(e) and 10(f). For **IBZ-EDA**, the chromaticity coordinates shift progressively from (0.16, 0.02) at 265 nm excitation to (0.35, 0.46) at 400 nm excitation. This pronounced movement across the CIE diagram reflects a substantial change in emission color from deep blue to green-yellow as lower-energy emissive states become increasingly dominant. In contrast, **IBZ-PHDA** exhibited a moderate chromaticity shift from (0.17, 0.01) at 265 nm to (0.26, 0.27) at 400 nm. Although a clear red-shift in the emission color is still observed, a smaller displacement indicates a comparatively narrower distribution of emissive states. These differences highlight the critical role of molecular architecture in controlling excited-state relaxation pathways. The flexible ethylene linker in **IBZ-EDA** appears to permit greater excited-state diversity and stronger excitation-dependent color tunability, whereas the rigid para-phenylene bridge in **IBZ-PHDA** imposes greater structural constraints, leading to a more restricted chromatic response.

The excitation-dependent shift in the apparent emission maximum observed for **IBZ-PHDA** was attributed to changes in the relative contributions of multiple emissive states rather than to a direct shift of a single fluorescence band. The coexistence of locally excited and charge-transfer-like states, together with the excitation-selective population of different emissive species, likely contributed to the observed spectral evolution. As the excitation wavelength increased from 350 nm to 400 nm, the emission profile evolved systematically, the long-wavelength emission component became progressively more dominant, and the short-wavelength band diminished. This behavior arises from the selective population of different excited-state conformations or configurations within a heterogeneous ensemble. In the case of **IBZ-PHDA**, the rigid *para*-phenylene linker restricts conformational relaxation, allowing excitation at longer wavelengths to preferentially populate molecules that are already pre-organized in geometries conducive to ICT from electron-rich benzoxazine to electron-deficient phthalimide. Conversely, excitation at shorter wavelengths results in a broader distribution of locally excited (LE) and ICT states, yielding emission spectra with contributions from both species. The systematic evolution of the emission profiles and the corresponding CIE chromaticity coordinates (Fig. 10f) confirmed that the observed spectral changes reflected genuine photoluminescence from multiple emissive states rather than experimental artifacts. This interpretation is further supported by the concentration-dependent emission behavior (Fig. 10b) and non-superimposable excitation spectra (Fig. 9d), which collectively demonstrate the coexistence of multiple emissive species with distinct excitation-emission relationships.

Overall, concentration-dependent and excitation-dependent fluorescence studies demonstrated that both **IBZ-EDA** and **IBZ-PHDA** possess complex excited-state landscapes involving multiple emissive species. The observed dual-emission behavior, concentration-enhanced long-wavelength fluorescence, excitation-dependent spectral evolution, and significant chromaticity modulation collectively indicate that intermolecular interactions and electronic communication between the benzoxazine and phthalimide units play central roles in governing the photophysical behavior of these monomers in solution.

*Solid-state photoluminescence properties of **IBZ-EDA** and **IBZ-PHDA***

To further elucidate the influence of molecular packing and intermolecular interactions on the photophysical behavior of the

synthesized benzoxazine monomers, the solid-state photoluminescence properties of **IBZ-EDA** and **IBZ-PHDA** in powder form were investigated under different excitation wavelengths. The resulting emission spectra and the corresponding CIE chromaticity coordinates are shown in Fig. 11. In contrast to the solution-state measurements discussed previously, where molecular species are largely isolated by the solvent environment, solid-state spectra reflect the combined effects of molecular aggregation, restricted intramolecular motions, through-space electronic interactions, and crystal or amorphous packing effects.

As shown in Figs. 11(a) and 11(b), both **IBZ-EDA** and **IBZ-PHDA** exhibit highly complex emission profiles in the solid state. The spectra were characterized by broad, intense, and excitation-dependent emission bands containing multiple overlapping maxima and shoulders distributed across the visible region. Although the spectral shapes differ significantly with the excitation wavelength, all emission profiles share a common feature: the coexistence of two principal emissive regions, one located in the shorter-wavelength region and a second extending into the longer-wavelength visible region. This dual-emission behavior is considerably more pronounced than that observed in dilute solutions, indicating that intermolecular interactions become increasingly important upon transitioning to the condensed phase.

For **IBZ-EDA**, excitation at 280 nm generated a particularly rich emission profile comprising multiple emissive components (Fig. 11a). The spectrum contained two dominant maxima located at approximately 383 and 522 nm, together with several less intense features centered near 363, 458, 485, and 497 nm. The appearance of numerous emission bands spanning a wide spectral range suggested the presence of multiple radiative relaxation channels within the solid matrix. The higher-energy emission centered in the blue-violet region is likely associated with locally excited states that may originate from individual benzoxazine-phthalimide segments, whereas the lower-energy emission centered near 522 nm may arise from intermolecularly stabilized excited states generated through molecular clustering and electronic interactions among neighboring chromophores. The simultaneous observation of these emissive components strongly suggests that the excited-state landscape of **IBZ-EDA** became substantially more heterogeneous in the solid state.

The strong excitation wavelength dependence observed in the solid state is consistent with the presence of heterogeneous emissive domains arising from multiple molecular

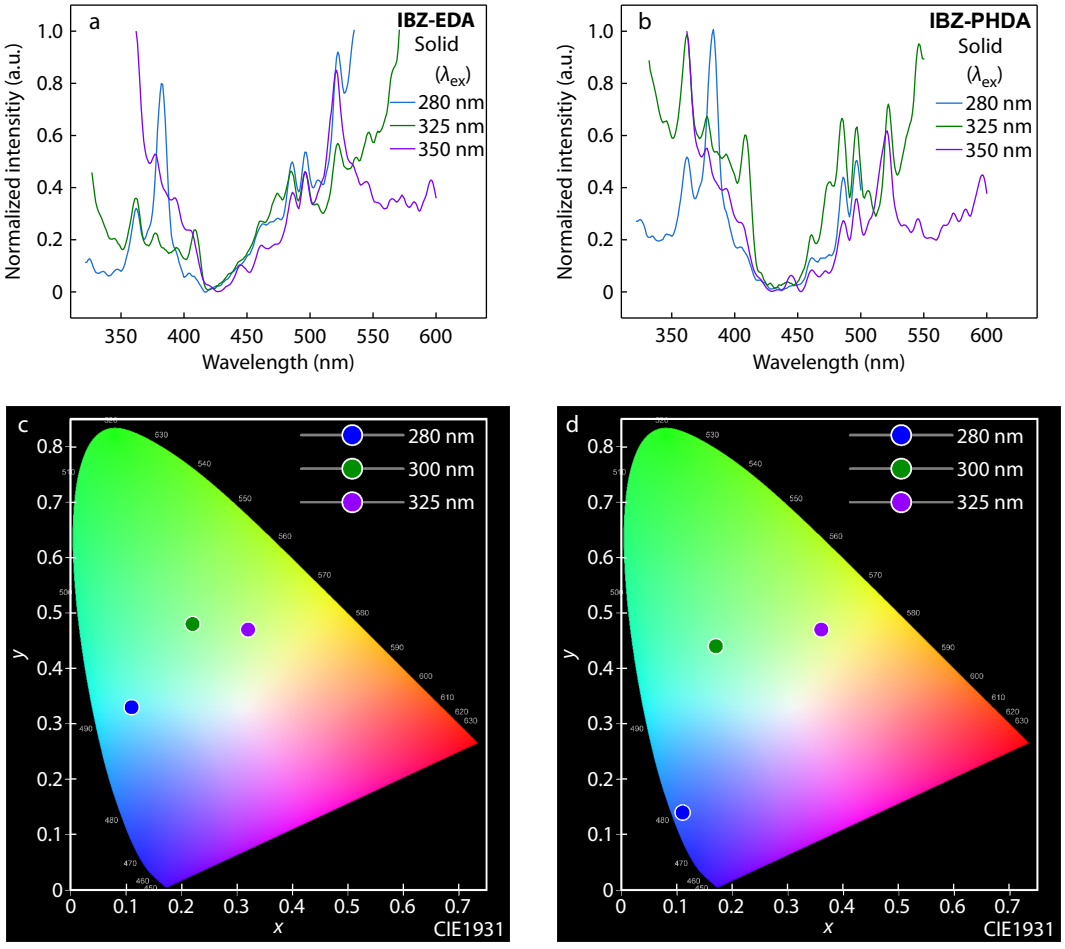

Fig. 11 (a) Solid-state emission spectra of **IBZ-EDA** powder recorded at λ_{ex} of 280, 300, and 325 nm; (b) Solid-state emission spectra of **IBZ-PHDA** powder recorded at λ_{ex} of 280, 300, and 325 nm; (c) Corresponding CIE chromaticity coordinates derived from the emission spectra of **IBZ-EDA** and (d) corresponding CIE chromaticity coordinates derived from the emission spectra of **IBZ-PHDA**.

https://doi.org/10.1007/s10118-026-3833-0

packing arrangements and intermolecular interactions. The higher-energy emission centered in the blue-violet region was tentatively assigned to locally excited states originating from individual benzoxazine-phthalimide segments, whereas the lower-energy emission centered near 522 nm may arise from intermolecularly stabilized excited states generated through molecular clustering and electronic interactions among neighboring chromophores. These assignments should be considered as possible interpretations consistent with the steady-state PL data, but definitive mechanistic conclusions would require additional spectroscopic validation, including time-resolved and temperature-dependent measurements.

The flexible ethylene bridge present in **IBZ-EDA** was expected to facilitate diverse molecular conformations and packing arrangements within the powder sample. This conformational variability can generate a broad distribution of intermolecular distances and interaction strengths, leading to the formation of multiple emissive microenvironments. The resulting electronic heterogeneity provides a plausible explanation for the large number of emission features observed in the visible spectrum. Furthermore, the restriction of intramolecular motions upon solidification may suppress nonradiative relaxation pathways, thereby enhancing the contribution of emissive states that remain weakly populated in the solution.

A similar complex behavior was observed for **IBZ-PHDA** (Fig. 11b), although the underlying origin is likely influenced by its more rigid molecular architecture. The para-phenylene linker imposes greater conformational rigidity and promotes more efficient electronic communication between benzoxazine-phthalimide units. Consequently, molecular packing in the solid state is expected to be more ordered than that of **IBZ-EDA**, potentially favoring stronger π–π interactions and enhanced through-space conjugation between neighboring molecules. The resulting excited-state manifold consisted of multiple emissive species whose relative contributions varied significantly with the excitation wavelength, producing distinct spectral profiles throughout the investigated excitation range.

An important feature of both monomers is the strong excitation wavelength dependence of the solid-state emission. The inability to superimpose the emission spectra obtained at different excitation wavelengths indicates that the fluorescence does not originate from a single emissive center. Instead, different excitation energies selectively populate distinct subsets of excited states, which subsequently relax *via* different radiative pathways. This behavior is frequently observed in systems containing heterogeneous emissive domains and is commonly associated with cluster-based luminescence mechanisms, excitation-dependent fluorescence, and through-space electronic coupling among heteroatom-rich molecular fragments. Considering the abundance of carbonyl oxygen atoms, ether oxygen atoms, and nitrogen centers in both monomers, the formation of various clustered electronic states in the solid phase is highly plausible.

Although the emission spectra of **IBZ-EDA** and **IBZ-PHDA** exhibit certain similarities at specific excitation wavelengths (*e.g.*, 280 nm), these similarities arise from the common phthalimide-benzoxazine chromophoric units that dominate the electronic transitions in both compounds. The material-dependent nature of the photophysical properties was evident when examining the full excitation-dependent evolution of the spectra. **IBZ-EDA** and **IBZ-PHDA** displayed distinct chromaticity trajectories (Figs. 11c and 11d) and different responses to excitation wavelength changes, reflecting the influence of the flexible ethylene versus rigid *para*-phenylene linker on molecular packing, intermolecular interactions, and excited-state relaxation pathways. The observed similarities at selected excitation wavelengths do not undermine the material dependence but rather highlight the contribution of the common chromophoric framework to the emission.

The structured emission profiles observed in the solid state, featuring multiple resolved maxima and shoulders, arise from a combination of vibronic progression, molecular packing effects, and exciton coupling between neighboring chromophores. The presence of multiple emissive bands reflects the heterogeneous distribution of molecular conformations and packing arrangements within the powder samples, which is consistent with previous reports on luminescent polybenzoxazines. The observation of structured emission in the solid state is a well-documented phenomenon in organic luminescent materials, and does not indicate stray light artifacts. All measurements were performed using long-pass filters in the emission path to eliminate scattered excitation light.

The CIE chromaticity diagrams presented in Figs. 11(c) and 11(d) provide additional evidence of the remarkable excitation-tunable emission characteristics of both compounds. For **IBZ-EDA**, the chromaticity coordinates shift from (0.11, 0.33) under 280 nm excitation to (0.22, 0.48) and (0.32, 0.47) under higher excitation wavelengths. This progressive displacement toward higher x and y values indicates a substantial increase in the contribution of the longer-wavelength emission components, resulting in a pronounced change in the perceived emission color. The broad chromaticity range reflects the coexistence of multiple emissive states with different spectral signatures and demonstrates the high sensitivity of the emission process to excitation energy.

A comparable trend is observed for **IBZ-PHDA**, whose chromaticity coordinates evolve from (0.11, 0.14) at 280 nm excitation to (0.17, 0.44) and ultimately (0.36, 0.47) at higher excitation wavelengths (Fig. 11d). The larger chromaticity displacement observed for **IBZ-PHDA** suggests that the rigid aromatic linker facilitates a more efficient population of lower-energy emissive states upon selective excitation. This behavior is consistent with the enhanced electronic coupling expected for the *para*-phenylene-bridged structure and supports the notion that molecular rigidity plays a critical role in determining the excited-state evolution in these systems.

The pronounced excitation-dependent fluorescence and broad chromaticity tunability observed for both monomers highlight the important role of intermolecular interactions in governing solid-state photophysical behavior. Relative to the solution state, where emissions are dominated primarily by isolated molecular species, the solid phase promotes the formation of multiple emissive domains through molecular packing and clustering effects. The coexistence of high-energy localized emission and lower-energy cluster-associated

emission produces the observed dual-emission characteristics and broad visible light coverage. These findings demonstrate that the photophysical properties of **IBZ-EDA** and **IBZ-PHDA** are strongly influenced by their molecular architecture and solid-state organization, providing valuable insights into the emission mechanisms operating within these imide-functional benzoxazine systems.

The strong excitation-wavelength dependence and the presence of multiple emission bands in the solid-state spectra reflect the heterogeneous nature of the emissive domains within the powder samples. This heterogeneity arises from several packing and microstructural features.

(i) Conformational heterogeneity: the flexible ethylenediamine linker in **IBZ-EDA** enables the molecule to adopt multiple conformations in the solid state, ranging from folded (where the two phthalimide-benzoxazine units are in close proximity) to extended (where they are separated). Each conformation creates a distinct local environment for the chromophores, resulting in different emission energies. For **IBZ-PHDA**, the rigid *para*-phenylene linker imposes greater conformational constraints, but variations in intermolecular packing (*e.g.*, slip angles, stacking geometries) still lead to heterogeneity. (ii) π–π stacking interactions: the abundant aromatic rings in both monomers engage in extensive π–π stacking interactions in the solid state. Different stacking geometries (H-aggregates versus J-aggregates) and intermolecular distances lead to varying degrees of exciton coupling and electronic communication, creating a distribution of emissive states with different energies. (iii) Hydrogen bonding networks: the heteroatom-rich molecular framework (imide carbonyl oxygen, ether oxygen, amine nitrogen, and phenolic —OH groups) forms a complex hydrogen-bonding network in the solid state. The diversity of hydrogen bond strengths and geometries creates a wide range of local electronic environments, each with distinct emission characteristics.

(iv) Coexistence of crystalline and amorphous domains: as confirmed by XRD analysis (Fig. 7), the powder samples contain both crystalline domains (ordered molecular packing) and amorphous domains (disordered molecular packing). The interfacial regions between these domains further contribute to the heterogeneity. (v) Through-space electronic interactions: the clustering of heteroatom-rich functionalities (carbonyl, ether, and amine groups) can facilitate through-space electronic interactions, generating cluster-associated emissive states with distinct excitation-emission relationships. (vi) Microscale surface features: the wrinkle patterns observed in the SEM images (Fig. 8) reflect microscale variations in stress distribution and crosslink density, creating local environments with different packing arrangements and emission properties.

Collectively, these factors generate a heterogeneous distribution of the emissive domains within the solid matrix. Upon excitation at different wavelengths, different subsets of these domains are selectively populated, resulting in an excitation-dependent emission behavior.

*Solid-state photoluminescence properties of **Poly(IBZ-EDA)** and **Poly(IBZ-PHDA)***

The photoluminescence properties of the thermally cured polymers, **Poly(IBZ-EDA)** and **Poly(IBZ-PHDA)** were investigated in the solid state, and the corresponding excitation-dependent emission spectra and CIE chromaticity coordinates are presented in Fig. 12. Owing to the highly crosslinked nature of the polybenzoxazine networks formed through thermally induced ring-opening polymerization (ROP), both polymers were insoluble in common organic solvents and, therefore, could only be examined in powder form. The observed emission behavior reflects not only the intrinsic electronic properties of the original monomeric building blocks, but also the profound structural and electronic modifications induced by polymerization.

Thermal curing converts the benzoxazine rings into a three-dimensional phenolic Mannich-bridge network, as illustrated in Scheme 1. This transformation introduces phenolic hydroxyl groups, increases the intermolecular connectivity, restricts molecular motion, and creates a heterogeneous distribution of local electronic environments throughout the polymer matrix. Consequently, the photophysical properties of the resulting polymers differ substantially from those of their corresponding monomers.

As shown in Fig. 12(a), **Poly(IBZ-EDA)** exhibited pronounced excitation-dependent fluorescence, characterized by significant variations in the spectral shape and emission distribution. Under excitation at 350 nm, the polymer displays intense short-wavelength emission below 400 nm, together with a dominant emission band centered near 480 nm, followed by a broad lower-energy emission extending beyond this wavelength. The coexistence of these emissive components suggests that multiple excited-state relaxation pathways were simultaneously active within the polymer network. The broad long-wavelength contribution indicated the presence of highly stabilized emissive states generated through intermolecular interactions and electronic coupling within the crosslinked matrix.

Upon excitation at 375 nm, the emission profile changed considerably, producing a dominant emission centered near 433 nm together with a secondary emission feature and a broad band extending throughout the 520–570 nm region. The emergence of this extended long-wavelength emission demonstrates that excitation at lower energies selectively populates the emissive states associated with more strongly coupled chromophoric domains within the polymer network. When the excitation wavelength was further increased to 400 nm, the emission evolved into a broad band spanning approximately 450–550 nm, accompanied by a substantial reduction in high-energy emission components. This progressive shift toward longer-wavelength fluorescence suggests that excitation at increasingly lower energies preferentially accesses the stabilized emissive states formed through intermolecular electronic interactions within the cured polymer structure.

Compared to the corresponding monomer **IBZ-EDA**, the polymer exhibited a markedly different emission pattern. In the monomeric state, the fluorescence is consistent with localized molecular excited states, together with concentration-dependent aggregate emission. Following polymerization, the formation of a rigid three-dimensional network significantly restricts intramolecular motion and enhances through-space interactions between the aromatic and heteroatom-containing moieties. The resulting suppression of non-radia-

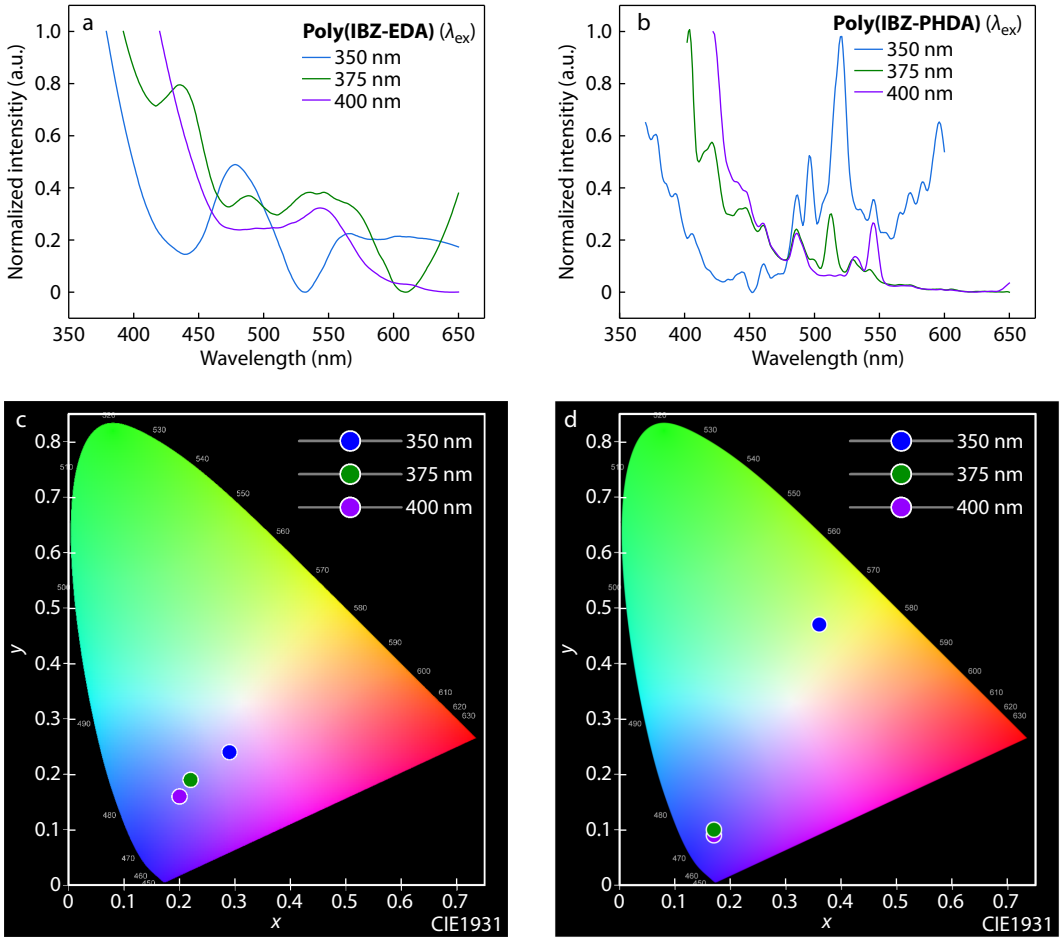

Fig. 12 (a) Solid-state emission spectra of **Poly(IBZ-EDA)** recorded at λ_{ex} of 350, 375, and 400 nm; (b) Solid-state emission spectra of **Poly(IBZ-PHDA)** recorded at λ_{ex} of 350, 375, and 400 nm; (c) Corresponding CIE chromaticity coordinates derived from the emission spectra of **Poly(IBZ-EDA)** and (d) corresponding CIE chromaticity coordinates derived from the emission spectra of **Poly(IBZ-PHDA)**.

tive relaxation pathways facilitated the generation of lower-energy emissive states, leading to the broad and excitation-dependent fluorescence observed in **Poly(IBZ-EDA)**.

The emission behavior of **Poly(IBZ-PHDA)** (Fig. 12b) differed substantially from that of **Poly(IBZ-EDA)** and more closely resembled the complex photophysical characteristics observed for the corresponding monomer. The spectra consisted of broad, feature-rich emission profiles with numerous overlapping maxima and shoulders across the visible region. The persistence of these highly structured emission patterns after polymerization suggests that the rigid *para*-phenylene linker continues to exert a strong influence on the electronic organization of the chromophoric units, even within the crosslinked network.

A particularly noteworthy feature of **Poly(IBZ-PHDA)** is the strong enhancement of long-wavelength emission under excitation at 350 nm. This behavior is reflected in the corresponding CIE chromaticity coordinates (0.36, 0.47), which represent the most red-shifted emission among all the excitation conditions investigated for this polymer. The enhanced contribution of the lower-energy emission bands suggests the efficient formation of stabilized emissive states associated with strong intermolecular interactions and extended electronic communication within the rigid polymer architecture. In contrast, excitation at 375 and 400 nm produced considerably bluer emissions, yielding chromaticity coordinates of (0.17, 0.10) and (0.17, 0.09), respectively. The substantial chromaticity shift induced by the excitation wavelength confirms the coexistence of multiple emissive species with distinct excitation-emission relationships.

The markedly different photoluminescence responses of **Poly(IBZ-EDA)** and **Poly(IBZ-PHDA)** highlight the critical role of the molecular architecture in governing excited-state processes after polymerization. The flexible ethylene spacer in **IBZ-EDA** likely generated a broader distribution of local conformations during network formation, producing heterogeneous emissive domains with varying degrees of electronic coupling. In contrast, the rigid para-phenylene bridge in **IBZ-PHDA** promotes a more constrained arrangement of chromophoric units, facilitating stronger electronic interactions and a more pronounced dependence of the emission color on the excitation energy.

The excitation-dependent fluorescence observed for both polymers further supports the existence of multiple emissive centers generated during network formation. In addition to conventional localized excited states, cured polymers contain abundant phenolic hydroxyl groups, tertiary amine centers, ether linkages, and imide carbonyl functionalities that

https://doi.org/10.1007/s10118-026-3833-0

can engage in extensive through-space electronic interactions. Clustering of these heteroatom-rich groups within the densely crosslinked polymer matrix can create a broad distribution of emissive states with different energy levels. It should be emphasized that while this interpretation is consistent with the observed excitation-dependent behavior, the exact nature of the emissive states cannot be unambiguously determined from steady-state PL measurements alone. Therefore, the proposed mechanisms are plausible interpretations that require further validation. Consequently, selective excitation at different wavelengths can preferentially populate distinct subsets of emissive centers, producing observed changes in the spectral profile and emission color.

The corresponding CIE chromaticity diagrams (Figs. 12c and 12d) clearly illustrate the remarkable tunability of emission properties following polymerization. For **Poly(IBZ-EDA)**, the chromaticity coordinates shifted from (0.24, 0.29) at 350 nm excitation to (0.22, 0.19) and ultimately (0.20, 0.16) at higher excitation wavelengths, indicating a gradual transition toward bluer emission. In contrast, **Poly(IBZ-PHDA)** exhibited a dramatic chromaticity change from (0.36, 0.47) at 350 nm to (0.17, 0.10) and (0.17, 0.09) at 375 and 400 nm excitation, respectively. Such large excitation-induced color variations demonstrate the complex excited-state landscape generated by polymerization and emphasize the strong influence of the network structure on the emissive behavior.

Overall, the solid-state photoluminescence results demonstrated that thermal ring-opening polymerization profoundly altered the emission characteristics of both monomers. The formation of highly crosslinked phenolic networks introduces new emissive environments, enhances intermolecular electronic interactions, and promotes excitation-dependent fluorescence over the broad visible range. The distinct emission behaviors of **Poly(IBZ-EDA)** and **Poly(IBZ-PHDA)** further revealed that the flexibility and rigidity of the bridging units play a crucial role in determining the nature of the emissive states generated within the cured polybenzoxazine matrices. These findings provide valuable insights into the structure–photophysical property relationships of imide-functional polybenzoxazines and highlight their potential as tunable solid-state luminescent materials.

CONCLUSIONS

In this study, two novel imide-functional benzoxazine monomers, **IBZ-EDA** and **IBZ-PHDA**, incorporating flexible ethylenediamine and rigid *para*-phenylenediamine bridging units, were successfully synthesized and comprehensively characterized. Structural elucidation using FTIR, NMR spectroscopy, and mass spectrometry confirmed the successful formation of the target benzoxazine architectures. Subsequent thermal ring-opening polymerization produced highly crosslinked polybenzoxazine networks, **Poly(IBZ-EDA)** and **Poly(IBZ-PHDA)**, the formation of which was verified by DSC and FTIR analyses.

The molecular architecture exerted a pronounced influence on the curing behavior and thermal performance of the resulting materials. **IBZ-EDA** exhibited a lower polymerization temperature because of the flexibility of the ethylenediamine spacer, whereas the rigid aromatic structure of **IBZ-PHDA** promoted the formation of a thermally robust network. Thermogravimetric analysis demonstrated remarkable improvements in thermal stability upon curing, particularly for **Poly(IBZ-PHDA)**, which achieved a T_{10} value of 559 °C, a char yield of 79%, and an LOI of 49.1%, indicating exceptional flame-retardant performance. SEM investigations further confirmed the formation of densely crosslinked thermoset networks and revealed distinct microstructural features governed by the linker rigidity.

Photophysical studies have revealed complex and highly tunable luminescent behavior in both solution and solid states. Concentration-dependent and excitation-dependent fluorescence measurements demonstrated the existence of multiple emissive states arising from the localized excited states, intermolecular interactions, and cluster-associated emission processes. Both monomers exhibited dual-emission characteristics and significant chromaticity modulation, whereas solid-state measurements highlighted the critical role of molecular packing and through-space electronic interactions. Following polymerization, the formation of highly crosslinked phenolic networks generates new emissive environments and enhances excitation-dependent fluorescence. Notably, the rigid **Poly(IBZ-PHDA)** network displayed the strongest long-wavelength emission contribution and the largest excitation-induced color variation.

Overall, this study establishes clear structure–property relationships linking molecular flexibility, network architecture, thermal stability, flame retardancy, and photophysical behavior in imide-functional benzoxazine systems. The combination of the outstanding thermal performance and tunable luminescence highlights the potential of these materials for advanced applications in high-performance thermosets, flame-retardant coatings, optical materials, sensing platforms, and luminescent functional polymers.

Conflict of Interests

The authors declare no interest conflict.

Electronic Supplementary Information

Electronic supplementary information (ESI) is available free of charge in the online version of this article at http://doi.org/10.1007/s10118-026-3833-0.

Data Availability Statement

The related data will be made available on request from the corresponding author.

ACKNOWLEDGMENTS

Abdulsalam Mahdy extends his gratitude to the University of Jordan, Chemistry Department, School of Sciences, for hosting his fellowship and providing funding support through the IIE-SRF program. One of the authors (HKJ) thanks the School of Scientific Research at the University of Jordan for granting him Sabbatical leave. Osama Younis gratefully acknowledges

support from the National Scholarship Programme of the Slovak Republic (SAIA). DeepSeek AI was used for language polishing. The final manuscript content and accuracy were thoroughly checked and are the sole responsibility of the authors.

REFERENCES

1 Li, S.; Zhou, J. H.; Han, S. L.; Wang, D.; Yu, Y. Y.; Li, J. Y.; Liu, S. H.; Chen, X.; Yang, X.; Sun, J.-K. Interfacial charge-regulated microenvironments enabled by ionic organic cages for boosting electrocatalytic nitrate reduction to ammonia. *Angew. Chem. Int. Ed.* **2026**, *65*, e4155022.

2 Xie, X.; Zhong, Y.; Muthukumar, P.; Zhang, B.; Yang, J.; Sun, J. K.; Yang, X.; Cheng, H. M. Enzyme-mimicking metal–phosphide tandem catalytic centers for efficient electrochemical nitrate-to-ammonia conversion and zinc–nitrate battery. *Angew. Chem. Int. Ed.* **2026**, *65*, e25416.

3 Wang, D.; Sun, Q.; Muthukumar, P.; Zhou, T.; Zhang, B.; Zhang, Q.; Yang, X.; Cheng, H. M. Unsaturated Cu single-atom catalysts in COFs for efficient neutral ammonia electrosynthesis from nitrate. *ACS Sustainable Chem. Eng.* **2026**, *14*, 3342–3353.

4 Mahdy, A.; Zahra, J. A.; Kasabri, V.; Haddadin, R. N.; Younis, O. A versatile platform of Quinolinoxazine monomers and polymers: unlocking structure-property relationships in thermal stability, biological activity, and white-light emission. *React. Funct. Polym.* **2026**, *221*, 106647.

5 Ohashi, S.; Ishida, H. Various synthetic methods of benzoxazine monomers. In *Advanced and Emerging Polybenzoxazine Science and Technology*. Ishida, H., Froimowicz, **2017**, Elsevier, pp. 3–8.

6 Yadav, S.; Amarnath, N.; Lochab, B. Advancing renewable amines: furan-derived polybenzoxazines. *ACS Appl. Polym. Mater.* **2024**, *6*, 15281–15292.

7 Younis, O.; Khamies, A.; Yang, X.; Aly, K. I. Luminescent polybenzoxazine: synthesis, characterization, and photophysical properties. *Polym. Adv. Technol.* **2024**, *35*, e6521.

8 Akkus, B.; Zhu, H.; Mitsuishi, M. Bio-based benzoxazine-containing polycyclosiloxanes as flame-retardant adhesive materials. *ACS Appl. Polym. Mater.* **2024**, *6*, 9466–9476.

9 Yang, Z.; Xie, Z.; Zhang, Y.; Chen, H.; Tang, Z.; Sha, X.-L. Fully bio-based benzoxazine adhesive with enhanced strength *via* synergistic supramolecular and covalent cross-linking. *ACS Appl. Polym. Mater.* **2024**, *6*, 12897–12905.

10 Gorbunova, E. A.; Soboleva, L. A.; Shutov, V. V.; Gorlov, M. V.; Kireev, V. V.; Sirotin, I. S. Structure–property relationship of diaminodiphenylmethane-based Benzoxazines—Precursors for high-performance thermoset polymers. *ACS Appl. Polym. Mater.* **2024**, *6*, 11103–11109.

11 Stępień, M.; Nizioł, E.; Gazińska, M.; Marszałek-Harych, A.; Zierkiewicz, W.; John, Ł.; Wytrych, P.; Ejfler, J. Polymerization case with hydroxybenzoxazines: what is the role of the hydroxy group, does it act as a self-catalyst or a modifier of the polymer structure. *Macromolecules* **2025**, *58*, 473–487.

12 Mohamed, M. G.; Mahdy, A.; Obaid, R. J.; Hegazy, M. A.; Kuo, S.-W.; Aly, K. I. Synthesis and characterization of polybenzoxazine/clay hybrid nanocomposites for UV light shielding and anti-corrosion

Graphical Abstract

Soft and Rigid Imide-based Benzoxazines as Precursors to High-performance Polybenzoxazines: Synthesis, Thermal Behavior, and Tunable Photoluminescent Properties

Abdulsalam Mahdy, Jalal A. Zahra, Hassan K. Juwhari, Ruba I. Alzubi, and Osama Younis

The University of Jordan, Jordan; Albaydha University, Yemen; Ar-Rasheed Smart University, Yemen; Jordan Atomic Energy Commission, Jordan; New Valley University, Egypt; Slovak Academy of Sciences, Slovakia

Flexible and rigid imide-functional benzoxazines were synthesized and thermally polymerized into highly crosslinked polybenzoxazines with exceptional thermal stability, flame retardancy, and excitation-dependent tunable photoluminescence, demonstrating the crucial role of linker rigidity in governing multifunctional material performance.

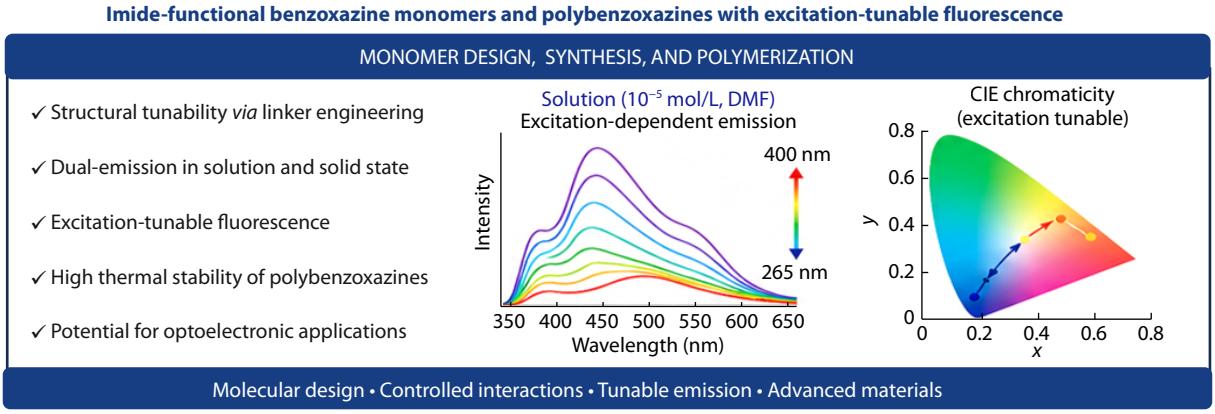

Chinese J. Polym. Sci. 2026 *https://doi.org/10.1007/s10118-026-3833-0*

coatings on mild steel. *J. Polym. Res.* **2021**, *28*, 297.
13 Aly, K. I.; Mahdy, A.; Hegazy, M. A.; Al-Muaikel, N. S.; Kuo, S.-W.; Gamal Mohamed, M. Corrosion resistance of mild steel coated with phthalimide-functionalized polybenzoxazines. *Coatings* **2020**, *10*, 1114.
14 Mahdy, A.; Zahra, J. A.; Haddadin, R. N.; Al-Hiari, Y.; Kasabri, V. Multi-biological activity evaluation of Sn(Π), Zn(Π) and Fe(Π) complexes based on thiocarbohydrazide schiff bases: synthesis, spectroscopic investigations and fluorescence studies. *Sci. Rep.* **2025**, *15*, 31757.
15 Kong, K.; MacKenzie, R.; Eaton, M.; Kibble, E.; Kanari, K.; Stafford, D.; Cooper, S.; Hamerton, I. Examining the effects of simulated low earth orbit on the viscoelasticity and strain behaviour of deployable polybenzoxazine nanocomposites. *Compos. Part A Appl. Sci. Manuf.* **2026**, *200*, 109362.
16 Yang, Y.; Lu, Y.; Chen, L.; Jing, Y.; Zhang, K. Recyclable, highly thermally stable and intrinsically flame retardant bio-based polybenzoxazine vitrimers enabled by dual dynamic covalent bonds. *Angew. Chem.* **2026**, *138*, e8806571.
17 Nunwong, C.; Luengrojanakul, P.; Charoensuk, K.; Rimdusit, S. Development of shape memory polybenzoxazines through copolymerization of conventional bisphenol-a benzoxazine with cardanol-based benzoxazine and their properties. *Polym. Bull.* **2026**, *83*, 262.
18 Chen, Q.; Ren, D.; Sheng, W.; Zhang, K. Synthesis, polymerization and thermal properties of bio-based benzoxazine resins containing imide or amide functionality. *J. Appl. Polym. Sci.* **2024**, *141*, e54792.
19 Mahdy, A.; Aly, K. I.; Mohamed, M. G. Construction novel polybenzoxazine coatings exhibiting corrosion protection of mild steel at different concentrations in a seawater solution. *Heliyon* **2023**, *9*, e17977.
20 Zhang, S.; Ran, Q.; Gu, Y. Polymerization mechanism of 1, 3-benzoxazine catalyzed by PCl_5 and rearrangement of chemical structures. *Eur. Polym. J.* **2021**, *142*, 110133.
21 Soto, M.; Hiller, M.; Oschkinat, H.; Koschek, K. Multifunctional benzoxazines feature low polymerization temperature and diverse polymer structures. *Polymers* **2016**, *8*, 278.
22 Mahdy, A.; Zahra, J. A.; Haddadin, R. N.; Kasabri, V.; Alkhaldi, H. S. Multifunctional cotton fabric treated with carboxylic acid–functionalized polynaphthoxazine/TiO_2 nanocomposites exhibiting enhanced UV protection, hydrophobicity, mechanical, and potential antibacterial activity properties. *Polym. Test.* **2026**, *159*, 109205.
23 Mahdy, A.; Al-Azzany, M.; Al-Hanany, S. A.; Al-Maweri, N. A.; Al-Ayzary, A. A. *In-situ* epoxidation of locally sourced sesame seed oil. *Albaydha Univ. J.* **2023**, *5*, 4.
24 Kim, H.-D.; Ishida, H. A study on hydrogen-bonded network structure of polybenzoxazines. *J. Phys. Chem. A* **2002**, *106*, 3271–3280.
25 Wang, C.-F.; Su, Y.-C.; Kuo, S.-W.; Huang, C.-F.; Sheen, Y.-C.; Chang, F.-C. Low-surface-free-energy materials based on polybenzoxazines. *Angew. Chem. Int. Ed.* **2006**, *45*, 2248–2251.
26 Zhang, K.; Liu, Y.; Han, L.; Wang, J.; Ishida, H. Synthesis and thermally induced structural transformation of phthalimide and nitrile-functionalized benzoxazine: toward smart *ortho*-benzoxazine chemistry for low flammability thermosets. *RSC Adv.* **2019**, *9*, 1526–1535.
27 Mahdy, A.; Zahra, J. A.; Haddadin, R. N.; Mohammed, A. A. K.; Mohamed, M. G. Molecular design and structural characterization of thiocarbohydrazide-derived azomethine-linked polybenzoxazine with antibacterial properties for cotton fabric applications. *J. Mol. Struct.* **2026**, *1352*, 144496.
28 Sheng, W.; Yin, R.; Chen, J.; Zhang, K. High-performance highly cross-linked networks based on ortho-imide functional mono-benzoxazines containing benzocyclobutene group. *React. Funct. Polym.* **2022**, *171*, 105154.
29 El-Mahdy, A. F. M.; Kuo, S. W. Direct synthesis of poly (benzoxazine imide) from an *ortho*-benzoxazine: its thermal conversion to highly cross-linked polybenzoxazole and blending with poly (4-vinylphenol). *Polym. Chem.* **2018**, *9*, 1815–1826.
30 Chen, W. C.; Kuo, S. W. *Ortho*-imide and allyl groups effect on highly thermally stable polybenzoxazine/double-decker-shaped polyhedral silsesquioxane hybrids. *Macromolecules* **2018**, *51*, 9602–9612.
31 Zhang, K.; Liu, J.; Ishida, H. An ultrahigh performance cross-linked polybenzoxazole *via* thermal conversion from poly(benzoxazine amic acid) based on smart *o*-Benzoxazine chemistry. *Macromolecules* **2014**, *47*, 8674–8681.
32 Zhang, K.; Ishida, H. An anomalous trade-off effect on the properties of smart ortho-functional benzoxazines. *Polym. Chem.* **2015**, *6*, 2541–2550.
33 Zhang, K.; Ishida, H. Smart synthesis of high-performance thermosets based on ortho-amideâ?"imide functional benzoxazines. *Front. Mater.* **2015**, *2*, 5.
34 Zhang, K.; Qiu, J.; Li, S.; Shang, Z.; Wang, J. Remarkable improvement of thermal stability of main-chain benzoxazine oligomer by incorporating *o*-norbornene as terminal functionality. *J. Appl. Polym. Sci.* **2017**, *134*, 45408.
35 Wang, M. W.; Lin, C. H.; Juang, T. Y. Steric hindrance control synthesis of primary amine-containing benzoxazines and properties of the resulting poly(benzoxazine imide) thermosetting films. *Macromolecules* **2013**, *46*, 8853–8863.
36 Mahdy, A.; Zahra, J. A.; Haddadin, R. N.; Kasabri, V.; Mohammed, A. A. K.; Mohamed, M. G. Multifunctional aliphatic diamine-based polynaphthoxazines: from synthesis and polymerization to bioactivity and photoluminescence. *ACS Omega* **2025**, *10*, 41878–41889.
37 Mahdy, A.; Zahra, J. A.; AlDamen, M. A.; Juwhari, H. K.; Younis, O. Substituent-engineered bifunctional naphthoxazines: tailoring thermal stability, morphology, and tunable photoluminescence in high-performance polybenzoxazines. *Eur. Polym. J.* **2026**, *248*, 114612.
38 Mahdy, A.; Al-Azzany, M. Synthesis, characterization and thermal properties of photoresponsive epoxy resin containing benzylidene units in the main chain. *Albaydha Univ. J.* **2022**, *4*, 159.
39 Sami, H.; Abozeed, A. A.; Tsutsumi, O.; Yang, X.; Younis, O. Influence of alkyl chain length and bromine substitution on thermal, photophysical, and optical properties of biphenyl luminescent molecules. *Opt. Mater.* **2025**, *159*, 116533.
40 Younis, O.; Harby, A.; Orabi, E. A.; Kamal El-Dean, A. M.; Sayed, M. M.; Tolba, M. S. Multifunctional polyamides: designing rigid and flexible architectures for flame retardant, dye adsorbent, single-material white-light emitting, and color-tunable photoluminescent systems. *React. Funct. Polym.* **2026**, *219*, 106597.
41 Younis, O.; Taher, F. M.; Sayed, M. M.; Sayed, M.; Ahmed, M. Naphthoxazine outperforms benzoxazine: carbazole-based polymers with enhanced blue luminescence and high thermal stability. *Eur. Polym. J.* **2026**, *243*, 114471.
42 Tolba, M. S.; Harby, A.; Kamal El-Dean, A. M.; Sayed, M. M.; Younis, O. Molecular engineering of polyhydrazides: a unified framework for tunable white-light emission, thermal robustness, and high-performance dye adsorption. *Eur. Polym. J.* **2026**, *246*, 114571.
43 Habib, T. G. F.; Zaki, R. M.; Kamal El-Dean, A. M.; Saddik, A. A.; Bishr, M.; Younis, O. Spacer-controlled crystallinity in phthalazine polymers: a unified route to tunable dye capture, flame resistance, and blue emission. *React. Funct. Polym.* **2026**, *226*, 106820.

44 Petrakova, V. V.; Kireev, V. V.; Onuchin, D. V.; Sarychev, I. A.; Shutov, V. V.; Kuzmich, A. A.; Bornosuz, N. V.; Gorlov, M. V.; Pavlov, N. V.; Shapagin, A. V.; Khasbiullin, R. R.; Sirotin, I. S. Benzoxazine monomers and polymers based on 3,3′-dichloro-4,4′-diaminodiphenylmethane: synthesis and characterization. *Polymers* **2021**, *13*, 1421.

45 Charisiadis, P.; Venianakis, T.; Papaemmanouil, C. D.; Primikyri, A.; Tzakos, A. G.; Siskos, M. G.; Gerothanassis, I. P. On the use of strong proton donors as a tool for overcoming line broadening in NMR: a comment. *Magn. Reson. Chem.* **2025**, *63*, 170–179.

46 Jamrozik, A.; Barczewski, M.; Framski, G.; Baranowski, D.; Jakubowska, P.; Klapiszewski, Ł.; Jesionowski, T.; Voelkel, A.; Strzemiecka, B. Synthesis and characterization of low-cost cresol-based benzoxazine resins as potential binders in abrasive composites. *Materials* **2020**, *13*, 2995.

47 Pang, T.; Zeng, M.; Feng, Z.; Chen, J.; Huang, Y.; Xu, Q. A facile method for the preparation of furfurylamine based benzoxazine resin with high-frequency low dielectric constants and ultra-low dielectric losses. *J. Mater. Sci. Mater. Electron.* **2019**, *30*, 8358–8370.

48 Ribeiro, F. W. M.; Silva-Oliveira, D.; Cervi, G.; Koyanagui, E. D.; Correra, T. C. Isomeric speciation of bisbenzoxazine intermediates by ion spectroscopy and ion mobility mass spectrometry. *ACS Omega* **2024**, *9*, 40932–40940.

49 Murai, Y.; Uemura, T.; Chen, Y.; Kawauchi, T.; Takeichi, T. Synthesis of high-molecular-weight benzoxazines from various combinations of bisphenols and diamines *via* Mannich condensation and properties of their thermosets. *Polym. J.* **2021**, *53*, 439–447.

50 Haubold, T. S.; Abels, G.; Koschek, K. A systematic study on the polymerization processes and resulting polymer properties of bioinspired sesamol and diamine-based benzoxazines. *J. Appl. Polym. Sci.* **2025**, *142*, e56497.

51 Demir, K. D.; Kiskan, B.; Aydogan, B.; Yagci, Y. Thermally curable main-chain benzoxazine prepolymers *via* polycondensation route. *React. Funct. Polym.* **2013**, *73*, 346–359.

52 Shukla, S.; Lochab, B. Role of higher aromatic content in modulating properties of cardanol based benzoxazines. *Polymer* **2016**, *99*, 684–694.

53 Davis, C.; Hollcraft, A.; Wiggins, J. Structure–property relationships of aryl ether diamine-based benzoxazines: role of aromatic substitution and molecular weight between crosslinks. *Polymers* **2026**, *18*, 440.

54 Fatima, K.; Gul, A.; Akhter, Z.; Rahman, R. Ferrocene based azo chromophore functionalized polyesters and its organic analogue: synthesis, structural elucidation, thermal behavior and IV characterization. *J. Inorg. Organomet. Polym. Mater.* **2017**, *27*, 474–480.

55 Coughlin, T.; Weng, K.; Salum, M. L.; Froimowicz, P.; Scott, C.; Ishida, H. Synthesis of umbelliferone-based, thermally stable, and intrinsically flame-retardant mono-oxazine benzoxazines: understanding the aminic moiety's influence on thermal properties. *Polymers* **2025**, *17*, 3340.

56 Telli, A. H. Preparation and characterization of polybenzoxazine involving various additives, Thesis, Middle East Technical University (Turkey), **2021**.

57 Ran, Q.; Gu, Y.; Ishida, H. Thermal degradation mechanism of polybenzoxazines. in *Advanced and emerging polybenzoxazine science and technology*. Amsterdam: Elsevier, **2017**, pp. 171–204.

58 Rojas-Rodriguez, M.; Rico-Martínez, S.; Prádanos, P.; Álvarez, C.; Alexandrova, L.; Lee, Y. M.; Lozano, Á. E.; Aguilar-Lugo, C. Thermally rearranged (TR) polybenzoxazoles from *o*-substituted precursor polyimides with phenyl pendant groups: synthesis, properties, and thermal rearrangement conditions. *Macromolecules* **2024**, *57*, 8187–8201.

59 Mohan, S.; Subramani, D.; Ammasai, K.; Muthukaruppan, A. Imidazole-core polybenzoxazine-silica hybrid composites *via* sol-gel approach: a new strategy for superior corrosion and flame resistance. *Next Mater.* **2025**, *9*, 101348.

60 Shukla, S.; Mahata, A.; Pathak, B.; Lochab, B. Cardanol benzoxazines–interplay of oxazine functionality (mono to tetra) and properties. *RSC Adv.* **2015**, *5*, 78071–78080.

61 Mandour, H. S. A.; Rehab, A.; Elnahrawy, M.; Salahuddin, N. Synthesis and characterization of chalcone based benzoxazine-magnetite nanocomposites. *Chem. Pap.* **2022**, *76*, 7565–7574.

62 Peyrefitte, J. J.; Hamernik, L. J.; Booker, E. M.; Arrington, J. D. Jr, Wiggins, J. S. Time scale-dependent structure–property relationships in dynamic imine-benzoxazine networks. *Macromolecules* **2026**, *59*, 503–514.

63 Asrafali, S. P.; Periyasamy, T.; Rafiqul Bari, G. A. K. M.; Lee, J. Properties of polybenzoxazine-based conducting materials in energy-related applications. *Polymers* **2025**, *17*, 2194.

64 Xin, C. L.; Li, G.; Yang, X.-P.; He, Y. D. Effect of inhomogeneous structure of polybenzoxazine on mechanical and thermal properties. *Adv. Mater. Res.* **2012**, *562/563/564*, 43–46.

65 Zhang, K.; Liu, J.; Ishida, H. High performance crosslinked polyimide based on main-chain type polybenzoxazine. *RSC Adv.* **2014**, *4*, 62550–62556.

66 Zhu, Z.; Chen, H.; Zhu, X.; Uenuma, S.; Ito, K.; Kotaki, M.; Sue, H.-J. Fracture behavior of polybenzoxazine toughened by polyrotaxane molecules and core–shell rubber. *ACS Appl. Eng. Mater.* **2023**, *1*, 1048–1057.

67 Hamerton, I.; McNamara, L. T.; Howlin, B. J.; Smith, P. A.; Cross, P.; Ward, S. Toughening mechanisms in aromatic polybenzoxazines using thermoplastic oligomers and telechelics. *Macromolecules* **2014**, *47*, 1946–1958.

https://doi.org/10.1007/s10118-026-3833-0